

Solving and learning advective multiscale Darcian dynamics with the Neural Basis Method

Yuhe Wang* Min Wang†

Abstract

Physics-governed models are increasingly paired with machine learning for accelerated predictions, yet most “physics-informed” formulations treat the governing equations as a penalty loss whose scale and meaning are set by heuristic balancing. This blurs operator structure, thereby confounding solution approximation error with governing-equation enforcement error and making the solving and learning progress hard to interpret and control. Here we introduce the Neural Basis Method, a projection-based formulation that couples a predefined, physics-conforming neural basis space with an operator-induced residual metric to obtain a well-conditioned deterministic minimization. Stability and reliability then hinge on this metric: the residual is not merely an optimization objective but a computable certificate tied to approximation and enforcement, remaining stable under basis enrichment and yielding reduced coordinates that are learnable across parametric instances. We use advective multiscale Darcian dynamics as a concrete demonstration of this broader point. Our method produce accurate and robust solutions in single solves and enable fast and effective parametric inference with operator learning.

Keywords: neural basis method, operator learning, residual-error equivalence, parametric PDEs, coupled Darcy flow and transport, multiscale advection-diffusion problem

Introduction

Flow-transport coupling in multiscale porous materials [1, 2] pose major challenges for computational modeling, especially in parametric many-query settings [3, 4]. Governed by elliptic-parabolic and advective PDEs with heterogeneous coefficients, such coupled dynamics entail conservation constraints, nonlinear effects, and multiscale interactions [5, 6]. Physics-informed machine learning [7], such as physics-informed neural networks (PINNs) [8, 9], is often presented as promising because it offers mesh-free approximations, seamless data integration, and potential learning-enabled acceleration. In practice, however, most approaches enforce physics through dimensionless L^2 loss minimization with heuristic weighting, which obscures physical scaling and disrupts numerical structure. This can yield poorly conditioned optimization in which approximation error is entangled with operator inconsistency, undermining accuracy and reliability [10–14]. This raises a fundamental question: where should physics and numerical structure reside in learning-based PDE models?

*Asia Pacific Technology, Inc., Houston, TX 77042, USA; Institute for Scientific Computation, Texas A&M University, College Station, TX 77843, USA. yuhe.wang@me.com

†Department of Mathematics, University of Houston, Houston, TX 77204, USA. mwang55@central.uh.edu

*†These authors contribute equally to this work.

In this work, we propose the Neural Basis Method (NBM), which departs from loss-driven training by seeking solutions through an explicit, deterministic procedure. We use predefined physics-conforming neural networks to construct finite-dimensional approximation spaces. Then, we impose PDEs by formulating a well-defined projection problem and solve for the solution coefficients. This design aligns NBM with classical numerical analysis and allows us to incorporate variational formulations [15] in a systematic and principled manner. Furthermore, for parametric cases, we represent solution families across parameter instances within the same neural space by learning the parameter-dependent solution coefficients, which naturally yields an operator learning formulation.

NBM is motivated by two lines of ideas: projection-based methods (e.g., Galerkin), which use fixed finite-dimensional space to enable stability, error control, and systematic refinement [16, 17], and neural approximation approaches, which offer expressive spaces for representing solution manifolds [18–20]. NBM therefore aims to integrate neural representations while retaining the structure and guarantees of projection-based schemes. Related ideas have recently appeared, including random feature and extreme learning machine-type methods, where fixed single-hidden-layer neural networks serve as basis functions and solution coefficients are obtained by least-squares [21–25]. They provide an important proof-of-concept, but the non-orthogonal bases often yield severely ill-conditioned least-squares systems [26–29]. Especially, for multiscale problems, resolving fine-scale structures requires basis enrichment [22, 30–32], which can drive rapid, often exponential, condition-number growth. NBM builds on this direction while departing in three ways: a multilayer neural basis generator that resists conditioning degradation under basis enrichment; an essential physical structure that is built in at vector field representation level; and a weighting and stabilization strategy that enforces consistency with the underlying operator and physical scaling. Our design draws on insights from least-squares finite element methods (LSFEM) and the discontinuous Petro-Galerkin (DPG) framework. LSFEM inspires properly scaled boundary residuals in seeking solutions via operator-residual minimization [33–36]. DPG theory connects optimal test norms for multiscale and advective problems to generalized least-squares formulations [37, 38]. Collectively, these insights motivate the NBM view that weighting and stabilization are treated as principled components of the projection-based approach rather than as heuristic loss balancing, preserving operator consistency and physical scaling and enabling reliable residual-based measures.

A direct consequence of this projection-based perspective is that NBM provides a built-in, physically meaningful measure of solution quality. This stands in contrast to the penalty losses used in many physics-informed neural approaches, whose magnitude and minimization depend sensitively on heuristic balancing and offer limited insight into operator consistency. In NBM, the residual serves as a numerically interpretable certificate tied to the discrete PDE enforcement, supporting systematic reasoning about approximation error. Thus, residual reduction can be interpreted within a projection framework analogous to classical schemes, enabling stability analysis and error assessment in the spirit of Galerkin theory, including Céa-type approximation properties. This residual-based notion of measure underpins the reliability of both solution accuracy and subsequent parametric inference built on the learned representation.

We then extend NBM from single instance solves to parametric operator learning (NBM-OL). In many query settings, including boundary/source control, performance optimization, and inverse modeling, the goal is to learn how the solution operator varies with governing parameters [39–41]. This necessitates a measure that is numerically comparable across parameters and, under stable projection, provides a computable a posteriori bound on the solution error [42, 43]. In NBM-OL, we learn parametric dependence in the fixed neural basis space equipped with such measure, instead of surrogate losses that lack direct numerical meaning. This provides a robust utility for monitoring

training and steering refinement across hyperparameters, with well-informed stopping criterion.

We present the first complete formulation and demonstration of NBM and NBM-OL in the setting of advective multiscale Darcian dynamics. For this coupled Darcy flow–transport system, we use physics-conforming neural vector bases in a nonlinear mixed Darcy flow formulation with energy-consistent weighting, and advance transport using a purely advective update stabilized by upwind control-volume treatment. Numerical experiments show accurate and stable single-instance solutions, and, for parametric inference, excellent in-distribution generalization, strong out-of-distribution robustness, and massive acceleration. In representative examples, we observe speedups on the order of 10^3 – 10^4 , and the gain scales with the prediction temporal horizon and problem size. Although we use a collocation-based realization for clarity and efficiency, our method also supports variational formulations, including DPG-inspired constructions with the optimal test theory that can provide theoretically optimal weighting and stabilization for multiscale and advective problems, with potential adaptive error control via the Riesz representation theorem [44]. A dedicated, DPG-inspired development of NBM is reported in subsequent, specialized work.

Results

We present the key progress of NBM development through an instantiation of coupled Darcy flow–transport in multiscale porous materials as a concrete testbed (descriptions in **Methods**). Using this context, we first summarize the key ingredients of NBM for solving the system; see Fig. 1. We next demonstrate NBM’s behavior on single-query setups. We then consider parametric many-query regimes, where variability arises from permeability fields and boundary values, and show how parametric inference is achieved through NBM-OL.

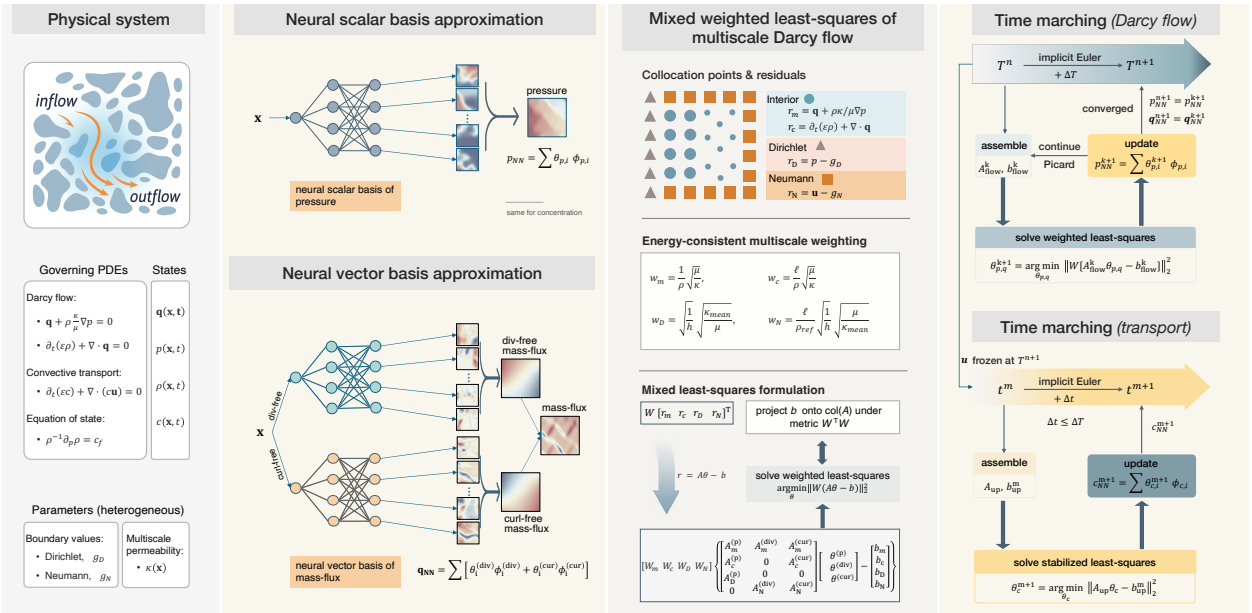


Fig. 1 | Overview of NBM as a neural PDE solver for coupled multiscale Darcy flow–transport. Left, Physical system. Middle-left, Neural basis approximation for scalar and vector field. Middle-right, Mixed weighted least-squares projection for multiscale Darcy flow. Right, Time marching of Darcy flow and transport.

Overview of NBM as a neural PDE solver

Core NBM formulation. NBM approximates solutions with finite neural basis functions and computes the solution coefficients through a PDE-constrained least-squares projection. For system (M1)-(M2), the pressure $p(\mathbf{x}, t)$ and mass-flux $\mathbf{q}(\mathbf{x}, t)$ are smooth and therefore suit global basis expansion naturally. In contrast, the concentration $c(\mathbf{x}, t)$ can develop limited regularity with discontinuous fronts and thus requires specialized stabilization or regularization. In general, we write $s_{NN}(\mathbf{x}, t) = \sum \theta_i(t) \phi_i(\mathbf{x})$, where a multilayer, fixed-parameter, ResNet-style network [45] generates the scalar spatial bases $\{\phi_i(\mathbf{x})\}$. Moreover, we let the coefficient vector $\boldsymbol{\theta}(t)$ carry temporal evolution. Here s denotes a scalar field, namely pressure, concentration, or a mass-flux component such as q_x or q_y . We freeze network weights/biases, so we defines a deterministic approximation space $\text{span}\{\phi_i\}$ and obtain the solution by projecting onto this space rather than by training the network. Specifically, we use two hidden layers to balance expressiveness and numerical conditioning while maintaining a clear geometric interpretation of the induced basis functions. We refer to this construction as a dual-layer neural basis; see **Methods** and **SI.2-5** for details. For the vector field \mathbf{q} , we propose a neural vector basis design inspired by the Helmholtz decomposition [46, 47] such that we approximate it as a sum of a divergence-free part $\phi_i^{(\text{div})}$ and curl-free part $\phi_i^{(\text{curl})}$,

$$\mathbf{q}_{NN} = \sum \left[\theta_i^{(\text{div})} \phi_i^{(\text{div})} + \theta_i^{(\text{curl})} \phi_i^{(\text{curl})} \right]. \quad (1)$$

We build the curl-free part as $\phi_i^{(\text{curl})} = \nabla \phi_i$, which represents the irrotational flow driven by potential. For the divergence-free part, we use a streamfunction formulation in 2D, $\phi_i^{(\text{div})} = \nabla^\perp \phi_i$, and a vector potential formulation in 3D, $\phi_i^{(\text{div})} = \nabla \times \mathbf{F}_i$, where \mathbf{F}_i can be constructed from the same scalar basis $\{\phi_i\}$; see **Methods** and **SI.7**. By this design, $\nabla \cdot \phi_i^{(\text{div})} = 0$ holds identically, so only the curl-free subspace enters the continuity equation (M2); it supplies the degrees of freedom needed to represent compressibility effects and source-driven mass redistribution, while the divergence-free component naturally captures mass-preserving motion. This physics-conforming representation preserves the intrinsic structure of fluid motion as much as possible at the representation level and can effectively improve solution accuracy (See **SI.6**). To compute the coefficient vector $\boldsymbol{\theta}$ at each time step or linearization iterate, NBM enforces (M4) via minimizer $\boldsymbol{\theta}^* = \arg \min_{\boldsymbol{\theta}} \|\mathcal{L}[\sum \theta_i \phi_i]\|_{\Omega}^2 + \|\mathcal{B}[\sum \theta_i \phi_i] - g\|_{\partial\Omega}^2$, which is linear in $\{\theta_i\}$ with $\{\phi_i\}$ being fixed. After neural discretization, it becomes $\boldsymbol{\theta}^* = \arg \min_{\boldsymbol{\theta}} \|\mathbf{A} \boldsymbol{\theta} - \mathbf{b}\|_{\mathbf{V}}^2$, where \mathbf{A} and \mathbf{b} encode the discretized PDE operators and boundary conditions under certain time stepping or linearization, and \mathbf{V} denote a properly-chosen norm in a general sense. In collocation-based realization we enforce the PDEs at collocation points, although NBM also supports variational or weak constructions. This minimization admits a projection interpretation: its residual is orthogonal to $\text{col}(\mathbf{A})$ under $\langle \cdot, \cdot \rangle_{\mathbf{V}}$, so we enforce the PDE constraints via a least-squares projection in the neural basis space. In practice, NBM removes nonconvex training altogether: at each update, $\boldsymbol{\theta}$ is obtained by solving a deterministic linear or linearized least-squares system, retaining the operator structure of classical schemes. Furthermore, under standard continuity and stability assumptions, this projection admits a probabilistic Céa-type bound: the error is controlled by the best approximation in the N_b -dimensional neural basis space, plus a high-probability $N_b^{-1/2}$ term, which is a conservative baseline guarantee; see Lemma 1 in **Methods**.

Mixed least-squares with energy-consistent weighting for multiscale Darcy flow. Discrete neural gradient and divergence operators are generally not adjoint. Consequently, a pressure-only approximation that eliminates \mathbf{q} through (M1) and then recovers it a posteriori does not, in general, preserve local mass conservation when inserted into (M2). We therefore devise a mixed

least-squares formulation and solve $\boldsymbol{\theta}_p$ and $\boldsymbol{\theta}_q$ simultaneously for each update by

$$\boldsymbol{\theta}_{p,q}^* = \arg \min_{\boldsymbol{\theta}_{p,q}} \left\{ \left\| \mathbf{q}_{NN} + \rho \frac{\kappa}{\mu} \nabla p_{NN} \right\|_{\Omega}^2 + \left\| \frac{\partial(\varepsilon\rho(p_{NN}))}{\partial t} + \nabla \cdot \mathbf{q}_{NN} \right\|_{\Omega}^2 + \|p_{NN} - p_D\|_{\partial\Omega_p}^2 + \|\mathbf{q}_{NN} \cdot \mathbf{n} - q_N\|_{\partial\Omega_q}^2 \right\}. \quad (2)$$

Here $\boldsymbol{\theta}_{p,q}$ denotes $(\boldsymbol{\theta}_p, \boldsymbol{\theta}_q)$, $p_{NN} = \sum_i \theta_{p,i} \phi_{p,i}$ and $\mathbf{q}_{NN} = \sum_i \theta_{q,i} \phi_{q,i}$, a compact form of (1). This mixed projection jointly enforces the constitutive law, the continuity constraint, and the boundary conditions, and produces locally conservative fluxes without a posterior correction. Here $\|\cdot\|_{\Omega/\partial\Omega}$ denotes a generic norm defined in Ω or on $\partial\Omega$, and its construction hinges on how we measure the interior and boundary residuals. Unweighted L^2 norms do not respect the Darcian energy scaling, which can degrade accuracy in multiscale media; this motivates energy-consistent weighting. Accordingly, we place all residual terms on a common Darcian energy scale: we weight the constitutive residual to match the dissipative metric $\int_{\Omega} \frac{\mu}{\kappa} |\mathbf{u}|^2 d\Omega$, and scale the continuity and boundary residuals to the same metric. Under collocation realization, this yields:

$$\boldsymbol{\theta}_{p,q}^* = \arg \min_{\boldsymbol{\theta}_{p,q}} \left\{ \left\| w_m \left(\mathbf{q}_{NN} + \rho \frac{\kappa}{\mu} \nabla p_{NN} \right) \right\|_{L^2(\Omega)}^2 + \left\| w_c \left(\frac{\partial(\varepsilon\rho(p_{NN}))}{\partial t} + \nabla \cdot \mathbf{q}_{NN} \right) \right\|_{L^2(\Omega)}^2 + \|w_D (p_{NN} - p_D)\|_{L^2(\partial\Omega_p)}^2 + \|w_N (\mathbf{q}_{NN} \cdot \mathbf{n} - q_N)\|_{L^2(\partial\Omega_q)}^2 \right\}, \quad (3)$$

with

$$w_m = \frac{1}{\rho} \sqrt{\frac{\mu}{\kappa}}, \quad w_c = \frac{\ell}{\rho} \sqrt{\frac{\mu}{\kappa_{\text{mean}}}}, \quad w_D = \sqrt{\frac{1}{h}} \sqrt{\frac{\kappa_{\text{mean}}}{\mu}}, \quad w_N = \frac{\ell}{\rho_0} \sqrt{\frac{1}{h}} \sqrt{\frac{\mu}{\kappa_{\text{mean}}}}. \quad (4)$$

In w_c and w_N , ℓ is a characteristic length that ensures dimensional consistency relative to the constitutive residual. The weights w_D and w_N balance the pressure and mass-flux boundary residuals against the interior energy scaling with a measure correction $\sqrt{1/h}$ to compensate for the codimension-one boundary sampling in collocation. Here h is the collocation spacing of the residual evaluation over the physical domain. κ_{mean} is the mean permeability and ρ_0 is the reference density. These weights measure all terms in compatible weighted L^2 norms and yield a consistent, physically interpretable projection. In a compact form under collocation (see **Methods**), we have

$$\boldsymbol{\theta}_{p,q}^* = \arg \min_{\boldsymbol{\theta}_{p,q}} \left\| \mathbf{W} (\mathbf{A}_{\text{flow}} \boldsymbol{\theta}_{p,q} - \mathbf{b}_{\text{flow}}) \right\|_2^2, \quad (5)$$

where \mathbf{W} is the weighting matrix comprised of (4). We then can define a residual measure in a relative sense as $\mathcal{E}_{\text{rel}} = \left\| \mathbf{W} (\mathbf{A}_{\text{flow}} \boldsymbol{\theta}_{p,q} - \mathbf{b}_{\text{flow}}) \right\|_2^2 / \left\| \mathbf{b}_{\text{flow}} \right\|_2^2$.

Upwind control-volume stabilization for transport. For transport, we treat the velocity field \mathbf{u}_{NN} as known and hold it frozen over each Darcy-flow update. To stabilize advection, we enforce (M3) using a control-volume collocation with first-order upwinding. This gives the following discrete balance for each control-volume K

$$\varepsilon \frac{c_{NN,K}^{m+1} - c_{NN,K}^m}{\Delta t} |K| + \sum_{f \in \partial K} (\mathbf{u}_{NN} \cdot \mathbf{n})_f c_{NN,f}^{m+1, \text{up}} |f| = 0, \quad (6)$$

where $c_{NN} = \sum_i \theta_{c,i} \phi_{c,i}$, $|K|$ denotes the measure of the cell K , $|f|$ denotes the measure of a face $f \subset \partial K$, and m is the time index for transport update. The sign of $(\mathbf{u}_{NN} \cdot \mathbf{n})_f$ selects the upwind state and defines $c_{NN,f}^{m+1,\text{up}}$. We assemble each face flux by evaluating the neural basis $\phi_{c,i}$ in the upwind cell. The inflow boundary concentration then enters (6) naturally as the corresponding upwind state, eliminating explicit boundary residuals. This construction yields a linear least-squares solve for each concentration update. By inheriting the stability of classical upwinding finite-volume schemes while retaining a global low-dimensional neural representation, it effectively suppresses the spurious oscillations that global bases often introduce in advective regimes. Similarly, we write its compact form under collocation

$$\boldsymbol{\theta}_c^* = \arg \min_{\boldsymbol{\theta}_c} \|\mathbf{A}_{\text{up}} \boldsymbol{\theta}_c - \mathbf{b}_{\text{up}}\|_2^2, \quad (7)$$

where \mathbf{A}_{up} and \mathbf{b}_{up} are assembled by applying the upwind control-volume balance (6) to each cell and its residual measure is thus $\mathcal{E}_{\text{rel}} = \|\mathbf{A}_{\text{up}} \boldsymbol{\theta}_c - \mathbf{b}_{\text{up}}\|_2^2 / \|\mathbf{b}_{\text{up}}\|_2^2$. This construction defines an advection-aware residual metric and can be interpreted as an implicit, generalized weighting, analogous in spirit to the energy-consistent weighting used for Darcy flow.

Implicit time integration and nonlinearity treatment. For Darcy flow, given p_{NN}^n at time T^n , we advance one Darcy time step ΔT to T^{n+1} by solving (5) with implicit time integration. For the nonlinearity induced by pressure-dependent density in (M1), we choose Picard linearization. At Picard iterate k , we update the coefficients by

$$\boldsymbol{\theta}_{p,q}^{k+1} = \arg \min_{\boldsymbol{\theta}_{p,q}} \left\| \mathbf{W}(\mathbf{A}_{\text{flow}}^k \boldsymbol{\theta}_{p,q} - \mathbf{b}_{\text{flow}}^k) \right\|_2^2, \quad (8)$$

where $\mathbf{A}_{\text{flow}}^k$ and $\mathbf{b}_{\text{flow}}^k$ are evaluated using the previous iterate p_{NN}^k . With $p_{NN}^{k+1} = \sum \theta_{p,i}^{k+1} \phi_{p,i}$ and $\mathbf{q}_{NN}^{k+1} = \sum \theta_{q,i}^{k+1} \phi_{q,i}$, we iterate until convergence and obtain $(p_{NN}^{n+1}, \mathbf{q}_{NN}^{n+1})$ at T^{n+1} . At the end of each Darcy step, we then advance transport from T^n to T^{n+1} with frozen velocity $\mathbf{u}^{n+1} = \mathbf{q}_{NN}^{n+1} / \rho_{NN}^{n+1}$. We use implicit time integration to overcome CFL restriction. However, to better resolve the advective front propagation, we take multiple transport substeps within $[T^n, T^{n+1}]$ because concentration generally evolves on much smaller time scale than Darcy flow. Consequently, for each transport substep $t^m \rightarrow t^{m+1}$ in $[T^n, T^{n+1}]$, we formulate (7) as

$$\boldsymbol{\theta}_c^{m+1} = \arg \min_{\boldsymbol{\theta}_c} \|\mathbf{A}_{\text{up}} \boldsymbol{\theta}_c - \mathbf{b}_{\text{up}}^m\|_2^2, \quad (9)$$

where \mathbf{A}_{up} is fixed, while \mathbf{b}_{up}^m collects the previous-step result together with the boundary inflow condition. Then, when $t^{m+1} = T^{n+1}$, we set $c^{n+1} = c^{m+1} = \sum \theta_{c,i}^{m+1} \phi_{c,i}$.

NBM produces advective Darcian solutions with spectral-like accuracy

For a homogeneous compressible Darcy–transport problem based on underground supercritical CO_2 storage (Fig. 2a), the residual \mathcal{E}_{rel} decays in two near-linear stages on semi-log scale as the neural basis size N_b increases: a rapid drop that resolves dominant structures, followed by a milder slope as higher-frequency features become harder to represent with a finite basis (Fig. 2b). Consistent with this behavior, the relative L_2 errors of pressure, velocity, and concentration decrease rapidly and remain competitive with FVM across all variables (Fig. 2c). The velocity statistics also converge in a spectral-like manner, as quantified by the Kolmogorov–Smirnov distance, and the qualitative fields show systematic refinement with increasing N_b (Fig. 2d–e). For fieldwise errors in pressure,

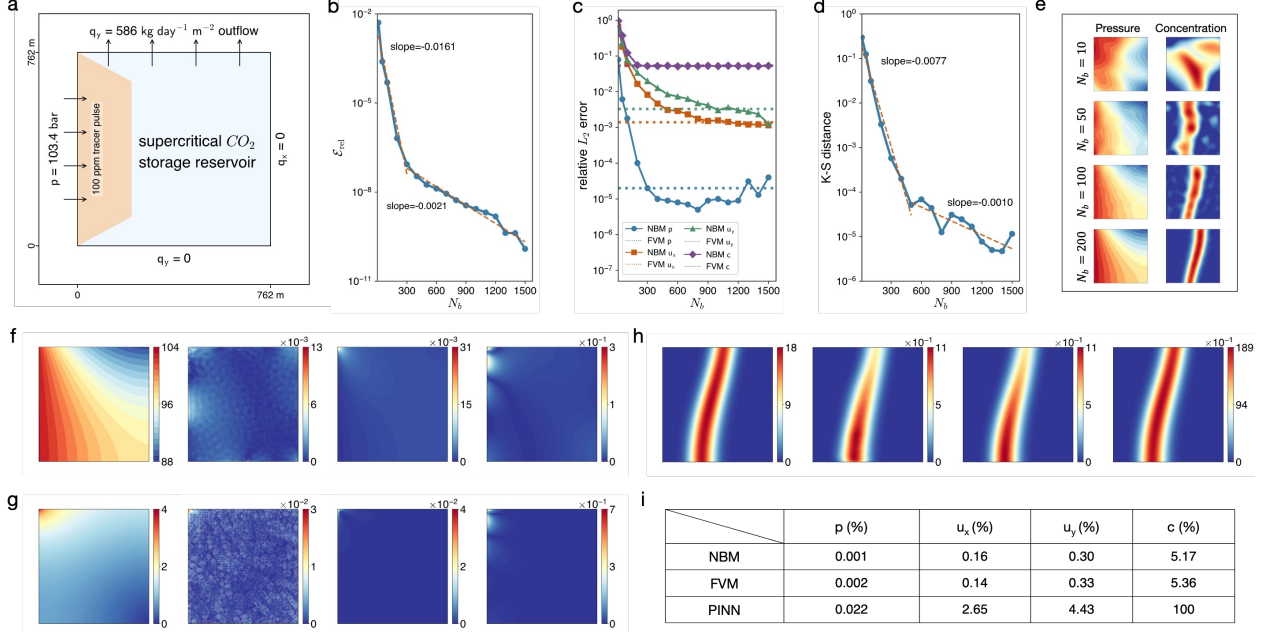


Fig. 2 | NBM solves advective Darcian system with spectral-like accuracy. **a**, Homogeneous CO_2 storage model. **b**, Residual \mathcal{E}_{rel} vs. neural basis size N_b . **c**, Relative L_2 errors vs. N_b . **d**, Kolmogorov–Smirnov distance of NBM velocity field vs. N_b . **e**, Refinement of NBM pressure and concentration fields with increasing N_b . **f**, Left to right: ground-truth pressure, followed by absolute error fields (w.r.t. ground truth) for NBM, FVM, and vanilla PINN. **g**, Left to right: ground-truth velocity magnitude, followed by absolute error fields (w.r.t. ground truth) for NBM, FVM, and vanilla PINN. **h**, Left to right: ground-truth concentration, followed by absolute error fields (w.r.t. ground truth) for NBM, FVM, and vanilla PINN. **i**, Relative L_2 errors. **Note:** All results are at 90 days. In f–i, NBM uses $N_b = 1000$, and all methods (NBM, FVM, and vanilla PINN) employ a 50×50 spatial resolution. Pressure is reported in bar, velocity in m day^{-1} , and concentration in ppm. See **Methods** for experiment details.

velocity, and concentration, we compare NBM against a finite-volume method (FVM) and a vanilla PINN. NBM attains a 0.001% relative L_2 error in pressure, about 50% lower than FVM (0.002%). For velocity, NBM yields 0.16% for u_x (FVM: 0.14%) and 0.30% for u_y (FVM: 0.33%), whereas the vanilla PINN underperforms (2.65% for u_x and 4.43% for u_y). For concentration, NBM (5.17%) closely matches FVM (5.36%), while the PINN degrades severely (100%) (Fig. 2f–i).

NBM remains accurate and robust for multiscale permeability fields

For this Darcy–transport problem but under a challenging multiscale permeability field (Fig. 3a), increasing the neural basis size N_b yields similar spectral-like residual decay together with systematic basis refinement (Fig. 3b–e). Using the FVM solution as a baseline, fieldwise comparisons show that energy-consistent weighting is critical in the multiscale regime: without weighting, the flow-field energy-spectrum discrepancy $E(k)$ increases from 0.91% to 7.05% ($7.7\times$ increase), and the transport solution driven by this flow field deteriorates sharply, with the concentration relative L_2 difference rising from 4.09% to 17.6% ($4.3\times$) (Fig. 3f–j). By contrast, a vanilla PINN fails to produce meaningful solutions. Because a ground-truth is unavailable for this discrete-valued permeability field, the FVM solution is used only as a comparison baseline; discrepancies relative to it should not be interpreted as inaccuracy of NBM. We therefore include a manufactured-solution benchmark with a separable multiscale permeability to assess multiscale accuracy and robustness. NBM exhibits the same decay trend while converging to more accurate solutions than FVM (Fig. 3l–m), and the energy spectra confirm that it matches the dominant low-frequency mode of the true

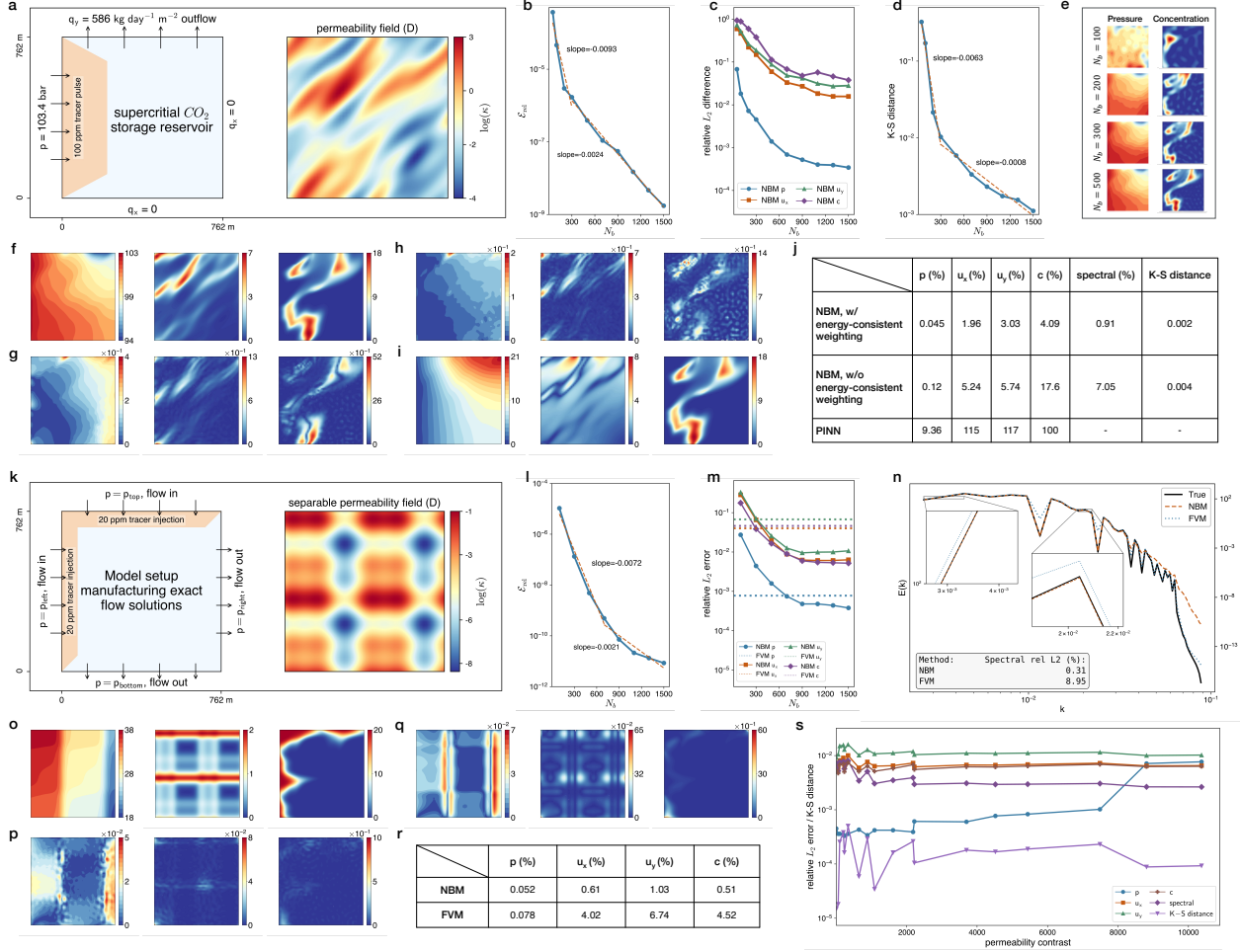


Fig. 3 | NBM remains accurate and robust for multiscale permeability fields. **a**, Multiscale CO₂ storage model. (permeability contrast 502). **b**, Residual \mathcal{E}_{rel} vs. neural basis size N_b . **c**, Relative L_2 difference vs. N_b . **d**, K-S distance vs. N_b . **e**, Refinement of NBM pressure and concentration fields with increasing N_b . **f**, Left to right: baseline pressure, velocity magnitude, and concentration. **g**, Left to right: absolute differences of NBM with energy-consistent weighting, for pressure, velocity magnitude, and concentration. **h**, Left to right: absolute differences of NBM without energy-consistent weighting, for pressure, velocity magnitude, and concentration. **i**, Left to right: absolute differences of PINN, for pressure, velocity magnitude, and concentration. **j**, Summary metrics measured against the baseline. **k**, Manufactured-solution setup (permeability contrast 1078). **l**, Residual \mathcal{E}_{rel} vs. N_b . **m**, Relative L_2 error vs. N_b . **n**, Energy spectrum $E(k)$ comparison. **o**, Ground-truth pressure, velocity magnitude, and concentration fields. **p**, Left to right: absolute errors of NBM, for pressure, velocity magnitude, concentration. **q**, Left to right: absolute errors of FVM, for pressure, velocity magnitude, concentration. **r**, Relative L_2 errors. **s**, Comparing metrics vs. permeability contrast. **Note:** Results in b–j are at 90 days. In f–j and o–s, NBM uses $N_b = 1000$, and all methods (NBM, FVM, and vanilla PINN) employ a 50×50 spatial resolution. Pressure is reported in bar, velocity in m day^{-1} , and concentration in ppm. See **Methods** for experiment details.

spectrum with much smaller spectral error (0.31% vs 8.95%) (Fig. 3n). NBM’s accuracy is also reflected in fieldwise errors: the relative L_2 errors drop from 0.078%/4.02%/6.74%/4.52% (FVM) to 0.052%/0.61%/1.03%/0.51% for (p, u_x, u_y, c) (Fig. 3o–r). Moreover, robustness to increasing permeability contrast is demonstrated up to 10^4 , with variable-wise and spectral relative L_2 errors and the K–S distance remaining controlled across the tested contrasts (Fig. 3s).

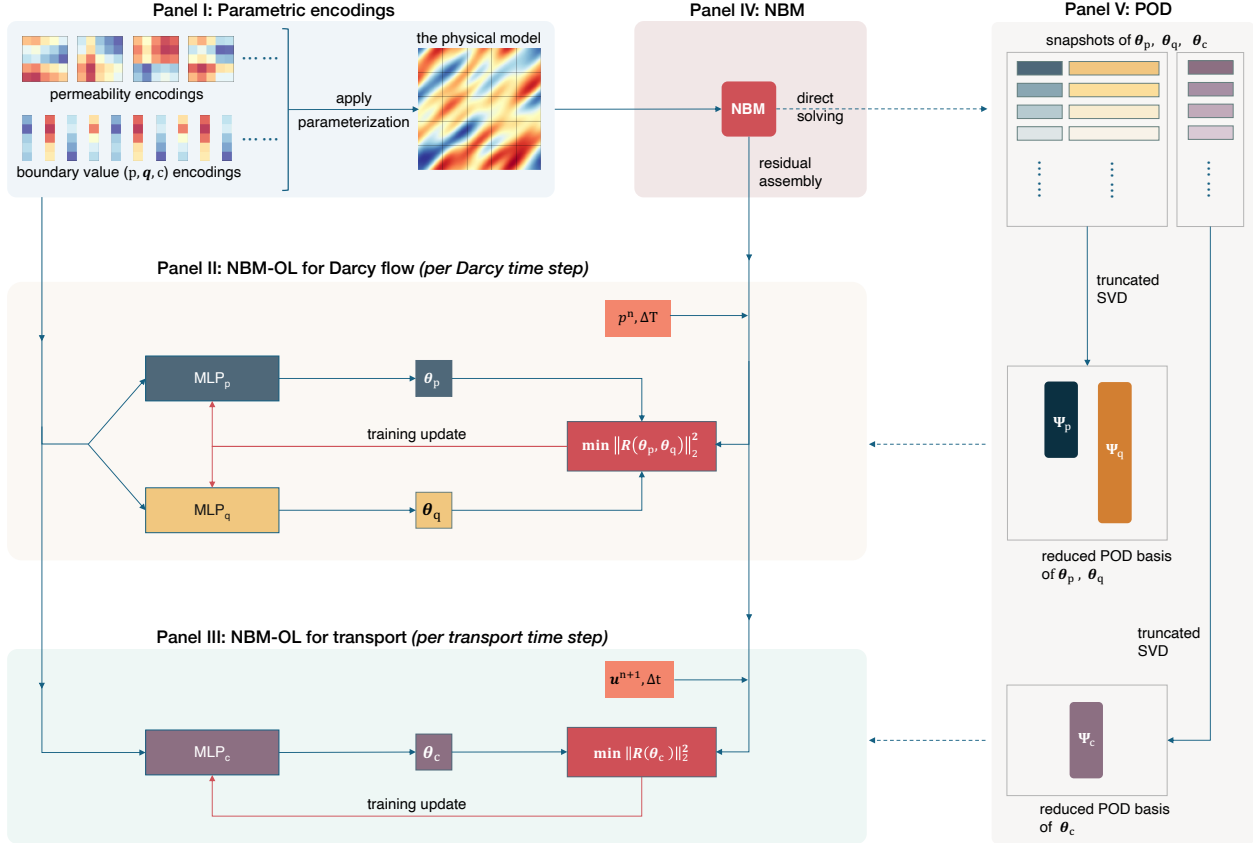
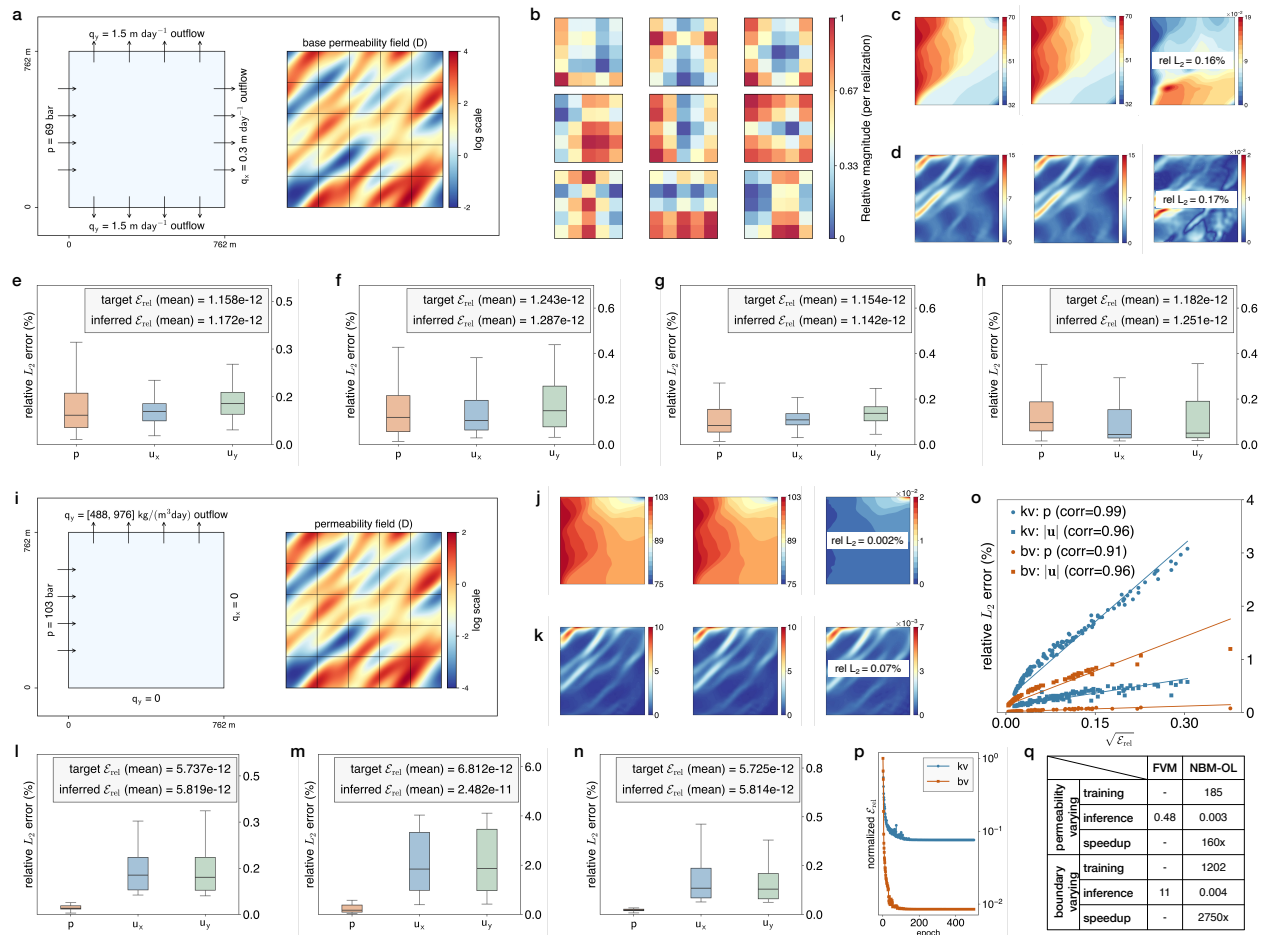


Fig. 4 | NBM-OL for parametric Darcy–transport systems. **Panel I**, Parameterization of permeability and boundary value. **Panel II**, NBM-OL for Darcy flow (per Darcy time step, ΔT). Two networks MLP_p and MLP_q learn the pressure and mass-flux solution coefficients θ_p and θ_q . Training is self-supervised by $\min \|\mathbf{R}(\theta_p, \theta_q)\|_2^2$ from (8), where $\mathbf{R}(\theta_p, \theta_q) = \mathbf{W}(\mathbf{A}_{\text{flow}} \theta_{p,q} - \mathbf{b}_{\text{flow}})$ with time stepping indices omitted. p^n denotes the pressure from the previous Darcy time-step, used for the current update. **Panel III**, NBM-OL for transport (per transport time-step, Δt). A dedicated network MLP_c learns concentration coefficients θ_c by $\min \|\mathbf{R}(\theta_c)\|_2^2$ from (9), where $\mathbf{R}(\theta_c) = \mathbf{A}_{\text{up}} \theta_c - \mathbf{b}_{\text{up}}$ with time stepping indices omitted. \mathbf{u}^{n+1} denotes the velocity after the current Darcy time-step update, computed as $\mathbf{u}^{n+1} = \mathbf{q}^{n+1}/\rho^{n+1}$. **Panel IV**, Optional POD compression of the solution coefficient snapshots. Ψ_p , Ψ_q , and Ψ_c are the respective reduced bases.

NBM enables effective operator learning for parametric Darcy flow–transport

The results above establish that NBM is accurate and robust, but solver-mode NBM requires dense least-squares solves. With basis size N_b and M residual evaluations, the computational cost scales as $\mathcal{O}(MN_b^2)$, so NBM is not intended to compete with highly optimized classical solvers in single-query settings. The situation changes in many-query regimes with parametric variations in PDE coefficients and boundary conditions, where repeated linear solves quickly become the bottleneck even for optimized solvers. NBM-OL addresses this regime by learning, offline, the parametric dependence of the solution coefficients in the predefined neural basis space and then evaluating them online at negligible cost. We use NBM-OL to learn the trajectory operator for the parametric Darcy–transport system (M5): parametric encodings, together with time when relevant, are mapped to the neural basis coefficients, as summarized in Fig. 4. The parametric inputs include heterogeneous permeabilities ξ_κ and boundary values ξ_b . To regularize learning and reduce dimensionality, we represent these inputs with low-dimensional encodings, as is standard in parametric PDE modeling [48]; for permeability, we use coarse blockwise parameters commonly adopted in geostatistical studies [49, 50]. The learned map predicts the neural basis coefficients,

interpreted as the reduced coordinates of the solution in the NBM space. Training is fully self-supervised and minimizes the same residuals (8) and (9) used by the NBM solver for flow and transport. Notably, each residual provides an interpretable certificate for monitoring, diagnosis, and improving the learning process. We show their equivalence to the respective state errors; see Lemma 2, 3 in **Methods**. When additional compression is beneficial, we optionally apply proper orthogonal decomposition (POD) to the solution coefficient trajectories to further reduce the operator output dimension. The following examples show that NBM-OL breaks the fundamental bottleneck of repeated parametric solves in many-query settings.



NBM-OL learns parametric Darcy flow operators under varying permeability and boundary flux. We apply NBM-OL to two parametric Darcy flow operators. Case-I isolates permeability variability in an incompressible setting, where the base permeability is parameterized by a piecewise-constant 5×5 coarse-block representation (block25), yielding a reduced operator family that preserves dominant spatial variability. Case-II isolates boundary control in the multi-scale CO₂ storage model, which is the uniform top-boundary mass-flux in [488, 976] kg/(m² day). Accuracy, robustness, and efficiency are summarized in Fig. 5. For Case-I, in-distribution generalization tests show consistently low relative L_2 errors for pressure and velocity (Fig. 5e). Robustness is further validated under out-of-distribution shifts that modify the heterogeneity level, correlation length, and spatial rotation; errors remain stable at the sub-percent level with only modest variance growth (Fig. 5f–h). For Case-II, in-distribution generalization tests yield tightly clustered sub-percent errors for pressure and velocity (Fig. 5l). Extrapolating the boundary-flux magnitude by 50% beyond the training range and extending the time horizon by 100% preserve accuracy and stability (Fig. 5m–n). During training, the normalized residual decays cleanly, and $\sqrt{\mathcal{E}_{\text{rel}}}$ linearly tracks solution L_2 errors across test cases, providing a calibrated accuracy proxy during learning; such an interpretable residual–error linkage is often unavailable in generic loss-driven operator learning. Finally, NBM-OL delivers the expected orders-of-magnitude speedups over FVM for parametric evaluation (Fig. 5q). See **Methods** and **SI.9** for detailed experiment setups.

NBM-OL learns parametric Darcy–transport operators under coupled flow and transport dynamics. Coupling transport with flow introduces sharp, hyperbolic dynamics that stress global reduced representations, making it a stringent test for operator learning. In this setting, both the boundary mass-flux and the injected tracer concentration are treated as parameters, using the same multiscale CO₂ storage configuration introduced earlier (Fig. 6). NBM-OL predicts concentration fields and tracks the evolving tracer fronts accurately (Fig. 6b–c). Sampling boundary flux and injected concentration within the training ranges yields tight, low-error distributions in in-distribution generalization tests (Fig. 6d). Extrapolating both parameter ranges by 50% and extending the time horizon by 100% increases errors only moderately, without instability or catastrophic degradation, indicating that the learned map captures the coupled flow–transport structure rather than narrow parameter memorization (Fig. 6e–f). The same residual–error alignment persists in the coupled flow–transport setting, with $\sqrt{\mathcal{E}_{\text{rel}}}$ linearly tracking concentration errors during training (Fig. 6g–h). Fast parametric rollout then follows from direct coefficient inference, yielding massive speedups over FVM (Fig. 6i). Experiment setups are provided in **Methods** and **SI.9**.

Discussion

NBM is a general, projection-based neural framework that unifies solving and learning PDE-based systems. Its central idea is to move physics out of heuristic loss-driven training and into the neural discretization itself through physics-conforming approximation spaces and operator-induced residual metrics. It yields a well-conditioned deterministic minimization, in which the resulting residual is a numerically meaningful certificate tied to both solution approximation and PDE enforcement. This gives stability under basis enrichment, supports systematic accuracy assessment, and produces reduced coordinates as natural targets for parametric learning. These coordinates can be learned consistently across parameter instances, while the residual certificate remains an interpretable measure for monitoring, diagnosis, and improving operator predictivity. Beyond the Darcy–transport instantiation, the new method applies whenever a PDE admits stable discrete enforcement under an appropriate residual norm. Although we experiment rather simplified parameterizations, NBM-OL

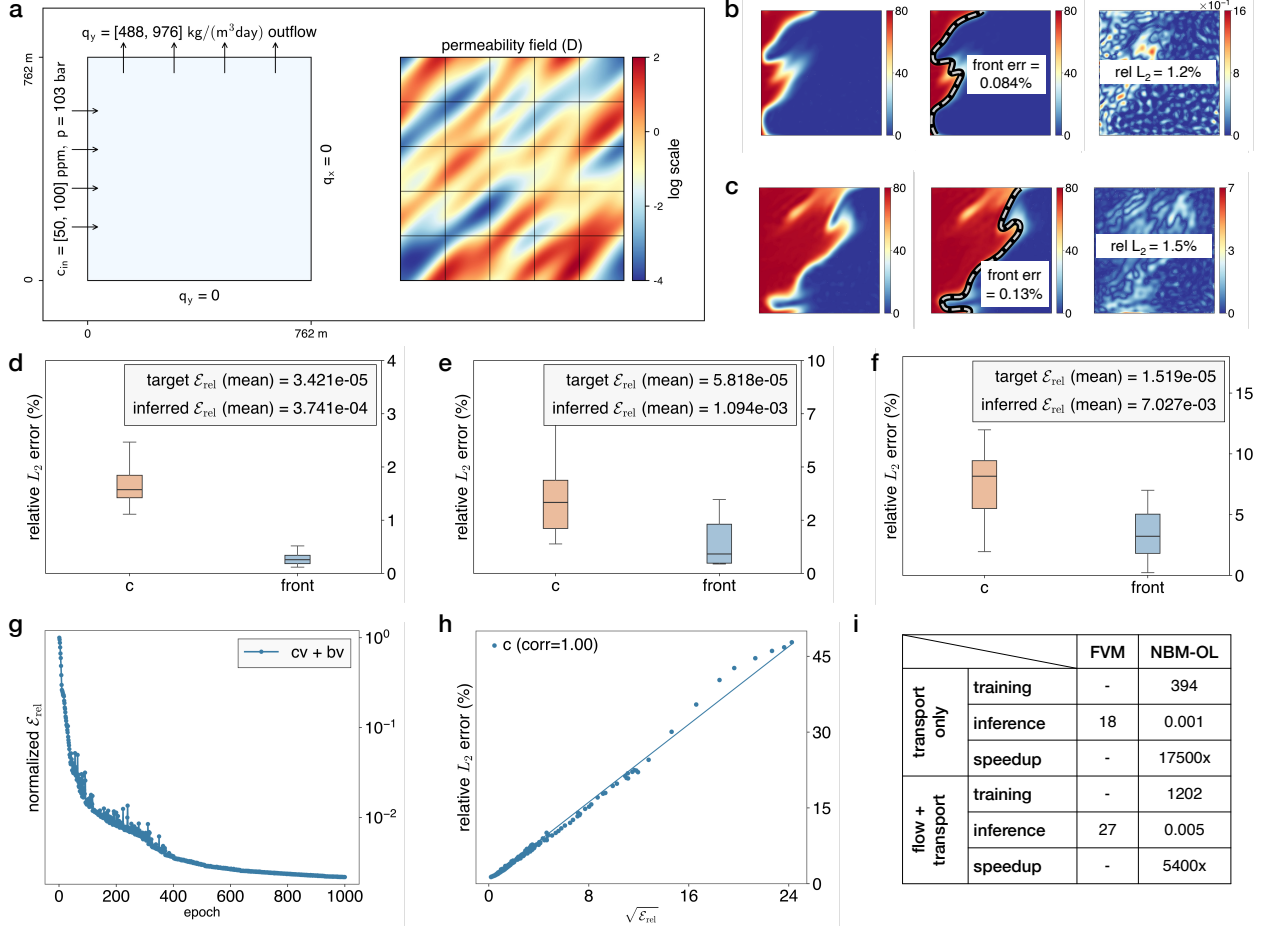


Fig. 6 | NBM-OL learns parametric Darcy-transport operators under varying boundary flux and concentration. **a**, Problem setup for boundary-flux-varying (bv) and injection-concentration-varying (cv) Darcy-transport operator learning. **b-c**, Left to right: true concentration, predicted concentration with the tracer front overlaid, and the corresponding absolute error; b is at 20 days and c is at 200 days. **d**, In-distribution generalization, measured by relative L_2 errors at 200 days over 100 random tests. **e**, Out-of-distribution generalization in boundary flux and concentration, measured by relative L_2 errors at 200 days over 100 random runs. **f**, Out-of-distribution generalization in time horizon, measured by relative L_2 errors at 400 days over 100 random runs. **g**, Training dynamics measured by normalized \mathcal{E}_{rel} . **h**, Residual-error correlation during training: $\sqrt{\mathcal{E}_{\text{rel}}}$ vs. relative L_2 errors. **i**, Runtime comparison and speedups of NBM-OL relative to FVM, reported as CPU wall-time statistics in seconds over 100 random runs. **Note**: Concentration is reported in ppm. See **Methods** for experiment details.

naturally extends to general parametric variations in operator coefficients, boundary conditions, and source terms, including spatially-varying and time-dependent profiles, enabling many-query tasks such as control, optimization, and inverse problems under parametric uncertainty.

There are several directions to further broaden robustness and generality. Our current neural bases are global and can struggle with localized non-smoothness or nonconvex geometries, where Gibbs-type artifacts [51] may cause loss of accuracy. NBM, however, is not limited to global representations and can be localized via domain decomposition, partition-of-unity, or spectral-element-style [52] global-local hybrids. The presented weighting and stabilization are based on strong-form collocation and should be viewed as a simplified, not optimal, choice. More rigorous variational constructions can draw on DPG-inspired designs. Within this umbrella, we can further benefit from residual localization via Riesz representers, yielding a computable error indicator that drives adaptive enrichment where the operator demands additional attention. In this way, NBM provides

not only a solver and surrogate, but also a diagnostic tool that guides modeling design. Measurements can also be appended as additional residual blocks to uncover system parameters, informed by model-data identifiability and compatibility. Finally, NBM is not intended to circumvent the curse-of-dimensionality in high-dimensional PDEs, where the number of basis functions can become impractical. Most PDEs in science and engineering, however, are posed on 1D-3D spatial domains, which is the regime NBM targets. Extending to fully 3D systems is thus another natural step, where scalable residual evaluation, randomized least-squares, and effective preconditioning warrant study.

Methods

Governing equations and problem definition

We consider a compressible fluid flow through a two-dimensional heterogeneous porous continuum. At the macroscopic scale, fluid motion is described by Darcy’s law, which provides a constitutive relation between pressure gradient and mass flux and is coupled with mass conservation:

$$\mathbf{q} + \rho \frac{\kappa}{\mu} \nabla p = 0, \quad (\text{M1})$$

$$\frac{\partial(\varepsilon\rho)}{\partial t} + \nabla \cdot \mathbf{q} = 0, \quad (\text{M2})$$

where $\mathbf{q}(\mathbf{x}, t)$ denotes the mass-flux, $p(\mathbf{x}, t)$ is the pressure, $\varepsilon(\mathbf{x})$ is the porosity, and $\rho(p)$ is the fluid density. The density is related to pressure through an equation of state, $\rho(p) = \rho_0(1 + c_f(p - p_0))$, where c_f is the fluid compressibility and ρ_0 is the reference density at reference pressure p_0 . The fluid viscosity μ and porosity ε are assumed constant, while $\kappa(\mathbf{x})$ is a spatially varying permeability tensor reflecting the heterogeneity of the medium. The Darcy velocity is defined as $\mathbf{u} = \mathbf{q}/\rho$. In addition to the flow equations, we consider a passive scalar field $c(\mathbf{x}, t)$ representing a transported concentration, which evolves according to the advection equation

$$\frac{\partial(\varepsilon c)}{\partial t} + \nabla \cdot (c \mathbf{u}) = 0, \quad (\text{M3})$$

and is assumed not to influence the flow field. For clarity of presentation, source terms in both the flow and transport equations are omitted, although they can be incorporated without modification of the formulation. With appropriate boundary conditions, equations (M1)–(M3) define a coupled Darcian flow–transport system that is conventionally solved in a sequential manner. The primary unknowns are chosen as the pressure p , the mass-flux \mathbf{q} , and the concentration c . Reference solutions are obtained using a finite-volume discretization, which is summarized in **SI.1**. For compactness, we express this dynamics in an operator form as

$$\begin{aligned} \mathcal{L}(s(\mathbf{x}, t)) &= 0 \quad \text{in } \Omega, \\ \mathcal{B}(s(\mathbf{x}, t)) &= g \quad \text{on } \partial\Omega, \end{aligned} \quad (\text{M4})$$

where $s(\mathbf{x}, t)$ denotes the collection of components from the primary unknowns. In addition to single-instance solving, we consider a parametric family of problems in which the governing operators depend on parameters. Specifically, we distinguish between parameters associated with the interior operator in terms of operator coefficients and those associated with the boundary operator,

$$\mathcal{L}_{\xi_\kappa}(s(\mathbf{x}, t)) = 0 \quad \text{in } \Omega, \quad \mathcal{B}_{\xi_b}(s(\mathbf{x}, t)) = g_{\xi_b} \quad \text{on } \partial\Omega, \quad (\text{M5})$$

where $\boldsymbol{\xi}_\kappa$ parameterizes variations in the permeability field and $\boldsymbol{\xi}_b$ parameterizes variations in boundary values. We collectively denote the full parameter vector by $\boldsymbol{\xi} = (\boldsymbol{\xi}_\kappa, \boldsymbol{\xi}_b)$. Equation (M5) defines a family of PDE systems sharing a common structure, which is the starting point for NBM-powered operator learning.

Dual-layer neural basis

We use a fixed-parameter, ResNet-style residual network with two hidden layers to construct the neural space $\{\phi_i(\mathbf{x})\}$. Let $\mathbf{x} \in \Omega \subset \mathbb{R}^d$ denote the spatial coordinate and let $\mathbf{x}_c \in \mathbb{R}^d$ be a fixed centering point (e.g., the domain center). The first hidden layer consists of N_1 nonlinear units $\phi_i^{(1)}(\mathbf{x}) = \sigma(\mathbf{w}_i \cdot (\mathbf{x} - \mathbf{x}_c) + b_i)$, where $\mathbf{w}_i \in \mathbb{R}^d$ and $b_i \in \mathbb{R}$ are fixed random parameters (weights and bias), and the activation is taken as $\sigma(\cdot) = \tanh(\cdot)$ in this work. Geometrically, each unit is associated with a characteristic hyperplane $\{\mathbf{x} : \mathbf{w}_i \cdot (\mathbf{x} - \mathbf{x}_c) + b_i = 0\}$; randomly oriented hyperplanes yield a statistically uniform partitioning of the domain and provide an interpretable geometric building block of the neural basis [15, 25, 53]. However, when used directly, the first-layer features may exhibit strong correlations under dense random sampling, which degrades the conditioning of the resulting projection systems, especially for multiscale operators. To obtain a numerically viable basis, we introduce a second hidden layer that applies a fixed linear–nonlinear recombination of the first-layer outputs, $\boldsymbol{\phi}^{(2)}(\mathbf{x}) = \sigma(\mathbf{W}_{\text{NN}}^{(2)} \boldsymbol{\phi}^{(1)}(\mathbf{x}) + \mathbf{b}_{\text{NN}}^{(2)})$, where $\boldsymbol{\phi}^{(1)}(\mathbf{x}) = (\phi_1^{(1)}(\mathbf{x}), \dots, \phi_{N_1}^{(1)}(\mathbf{x}))^\top \in \mathbb{R}^{N_1}$, $\mathbf{W}_{\text{NN}}^{(2)} \in \mathbb{R}^{N_2 \times N_1}$ and $\mathbf{b}_{\text{NN}}^{(2)} \in \mathbb{R}^{N_2}$ are the second-layer neural-network weight matrix and bias vector, and $\sigma(\cdot)$ acts componentwise. The inputs to this layer are precisely the hyperplane-induced features produced by the first layer. The nonlinear transformation reduces feature correlations and substantially improves numerical conditioning. We take the components of $\boldsymbol{\phi}^{(2)}(\mathbf{x})$ as the final scalar spatial basis functions such that $\phi_i(\mathbf{x}) = \phi_i^{(2)}(\mathbf{x})$; additional details are provided in **SI.2-5**.

Physics-conforming neural vector basis construction

The neural vector basis construction in 2D is rather straightforward. Given scalar neural bases $\{\phi_i(\mathbf{x})\}$, we define curl-free and divergence-free neural vector bases by

$$\boldsymbol{\phi}_i^{(\text{curl})}(\mathbf{x}) = \nabla \phi_i(\mathbf{x}) = \begin{bmatrix} \partial_x \phi_i(\mathbf{x}) \\ \partial_y \phi_i(\mathbf{x}) \end{bmatrix}, \quad \boldsymbol{\phi}_i^{(\text{div})}(\mathbf{x}) = \nabla^\perp \phi_i(\mathbf{x}) = \begin{bmatrix} \partial_y \phi_i(\mathbf{x}) \\ -\partial_x \phi_i(\mathbf{x}) \end{bmatrix}, \quad \mathbf{x} = (x, y),$$

so that $\nabla \times \boldsymbol{\phi}_i^{(\text{curl})} \equiv 0$ and $\nabla \cdot \boldsymbol{\phi}_i^{(\text{div})} \equiv 0$ hold identically. We approximate the mass-flux using (1), which yields the componentwise expressions

$$\begin{aligned} q_{x,NN}(\mathbf{x}) &= \sum \left[\theta_i^{(\text{div})} \partial_y \phi_i(\mathbf{x}) + \theta_i^{(\text{curl})} \partial_x \phi_i(\mathbf{x}) \right], \\ q_{y,NN}(\mathbf{x}) &= \sum \left[-\theta_i^{(\text{div})} \partial_x \phi_i(\mathbf{x}) + \theta_i^{(\text{curl})} \partial_y \phi_i(\mathbf{x}) \right]. \end{aligned}$$

Spatial derivatives of ϕ_i are evaluated via automatic differentiation of the neural basis generator. The same idea extends to 3D through a vector-potential representation $\boldsymbol{\phi}_i^{(\text{div})} = \nabla \times \mathbf{F}_i$ with \mathbf{F}_i constructed from $\{\phi_i\}$; see **SI.7** for the explicit form.

Approximation and stability properties of neural basis spaces

Lemma 1 (Probabilistic Céa-type bound for neural basis spaces). *Let V be a Hilbert space equipped with norm $\|\cdot\|_V$, and let $a(\cdot, \cdot) : V \times V \rightarrow \mathbb{R}$ be a continuous bilinear form with continuity constant*

$C_a > 0$ and stability constant $\gamma > 0$ (either coercive or inf-sup stable). Let $\{\phi_\omega\}_{\omega \sim \pi} \subset V$ denote a family of fixed neural basis functions parameterized by random variables ω drawn i.i.d. from a distribution π , and define the N_b -dimensional neural basis space

$$V_{N_b} := \text{span}\{\phi_{\omega_1}, \dots, \phi_{\omega_{N_b}}\} \subset V, \quad \omega_j \stackrel{\text{i.i.d.}}{\sim} \pi, \quad j = 1, \dots, N_b.$$

Let $u \in V$ be the exact solution of

$$a(u, v) = \ell(v), \quad \forall v \in V,$$

and let $u_{N_b} \in V_{N_b}$ denote the least-squares projection solution associated with the NBM formulation. Assume that u belongs to the reproducing kernel Hilbert space \mathcal{H}_k induced by the random neural basis construction, and that \mathcal{H}_k is continuously embedded in V ,

$$\|w\|_V \leq C_{\text{emb}} \|w\|_{\mathcal{H}_k}, \quad \forall w \in \mathcal{H}_k,$$

where C_{emb} is the embedding constant of $\mathcal{H}_k \hookrightarrow V$. Then, for any $\delta \in (0, 1)$, there exists a constant $C_1(\delta) > 0$ such that, with probability at least $1 - \delta$,

$$\|u - u_{N_b}\|_V \leq \frac{C_a}{\gamma} \left(\inf_{w \in \mathcal{H}_k} \|u - w\|_V + C_{\text{emb}} C_1(\delta) N_b^{-1/2} \right).$$

If, in addition, $u \in \mathcal{H}_k$ with $\|u\|_{\mathcal{H}_k} \leq B$, then

$$\|u - u_{N_b}\|_V \leq \frac{C_a}{\gamma} C_{\text{emb}} C_1(\delta) B N_b^{-1/2}.$$

Proof. By the C ea estimate associated with the Galerkin or least-squares projection, the NBM solution $u_{N_b} \in V_{N_b}$ satisfies

$$\|u - u_{N_b}\|_V \leq \frac{C_a}{\gamma} \inf_{w \in V_{N_b}} \|u - w\|_V. \quad (\text{M6})$$

Since $u \in \mathcal{H}_k$, classical results on Monte-Carlo approximation of kernel expansions (e.g., Rahimi-Recht or Bach-type bounds) imply that, for any $\delta \in (0, 1)$, with probability at least $1 - \delta$, there exists a function $v_{N_b} \in V_{N_b}$ such that

$$\|u - v_{N_b}\|_{\mathcal{H}_k} \leq C_1(\delta) \|u\|_{\mathcal{H}_k} N_b^{-1/2}. \quad (\text{M7})$$

Here v_{N_b} is a comparison function in V_{N_b} whose existence is guaranteed by random feature approximation theory and $C_1(\delta)$ is a constant depends on δ but is independent of N_b . Using the continuous embedding $\mathcal{H}_k \hookrightarrow V$, we obtain

$$\|u - v_{N_b}\|_V \leq C_{\text{emb}} \|u - v_{N_b}\|_{\mathcal{H}_k}. \quad (\text{M8})$$

Combining (M7) and (M8) yields

$$\|u - v_{N_b}\|_V \leq C_{\text{emb}} C_1(\delta) \|u\|_{\mathcal{H}_k} N_b^{-1/2}. \quad (\text{M9})$$

Since $v_{N_b} \in V_{N_b}$, by definition of the infimum,

$$\inf_{w \in V_{N_b}} \|u - w\|_V \leq \|u - v_{N_b}\|_V. \quad (\text{M10})$$

Substituting (M10) into the Céa's estimate (M6) and using (M9) gives

$$\|u - u_{N_b}\|_V \leq \frac{C_a}{\gamma} C_{\text{emb}} C_1(\delta) \|u\|_{\mathcal{H}_k} N_b^{-1/2}.$$

More generally, without assuming a bound on $\|u\|_{\mathcal{H}_k}$, the same argument yields

$$\|u - u_{N_b}\|_V \leq \frac{C_a}{\gamma} \left(\inf_{w \in \mathcal{H}_k} \|u - w\|_V + C_{\text{emb}} C_1(\delta) N_b^{-1/2} \right),$$

which completes the proof. \square

The above bound does not rely on symmetry of the operator. For the transport equation, the bilinear form $a(\cdot, \cdot)$ is generally non-symmetric but satisfies an inf-sup condition under appropriate least-squares norms. In such cases, the constant γ represents the corresponding inf-sup stability constant. Since the NBM formulation employs a deterministic least-squares realization, which can be interpreted as a Petrov–Galerkin projection, the same Céa-type estimate applies.

Collocation implementation of mixed weighted least-squares for multiscale Darcy flow

Each residual evaluation at a collocation point corresponds to one row of the discrete weighted least-squares system (5). For interior points $x_i \in \Omega$ with associated volume $|\Omega_i|$, we use $w_m(x_j) = 1/\rho \sqrt{\mu/\kappa(x_j)} \sqrt{|\Omega_j|}$ for the constitutive residual and $w_c(x_j) = \ell/\rho \sqrt{\mu/\kappa_{\text{mean}}} \sqrt{|\Omega_j|}$ for the continuity residual. For boundary points $x_b \in \partial\Omega$ with associated length or area $|\partial\Omega_b|$, we set $w_D(x_b) = \sqrt{1/h} \sqrt{\kappa_{\text{mean}}/\mu} \sqrt{|\partial\Omega_b|}$ and $w_N(x_b) = \ell/\rho_{\text{ref}} \sqrt{1/h} \sqrt{\mu/\kappa_{\text{ref}}} \sqrt{|\partial\Omega_b|}$. For collocation points that are uniformly distributed over Ω and $\partial\Omega$, the measures $|\Omega_i|$ and $|\partial\Omega_b|$ are straightforward to compute. Accordingly, the discrete residual vector takes the stacked form

$$\mathbf{r}(\boldsymbol{\theta}) = \begin{bmatrix} \mathbf{r}_m \\ \mathbf{r}_c \\ \mathbf{r}_D \\ \mathbf{r}_N \end{bmatrix} = \begin{bmatrix} \mathbf{A}_m \\ \mathbf{A}_c \\ \mathbf{A}_D \\ \mathbf{A}_N \end{bmatrix} \boldsymbol{\theta} - \begin{bmatrix} \mathbf{b}_m \\ \mathbf{b}_c \\ \mathbf{b}_D \\ \mathbf{b}_N \end{bmatrix}, \quad \boldsymbol{\theta} = \begin{bmatrix} \boldsymbol{\theta}^{(p)} \\ \boldsymbol{\theta}^{(\text{div})} \\ \boldsymbol{\theta}^{(\text{cur})} \end{bmatrix},$$

where $\mathbf{r}_m \in \mathbb{R}^{M_\Omega}$ and $\mathbf{r}_c \in \mathbb{R}^{M_\Omega}$ collect the constitutive and continuity residuals at interior collocation points, and $\mathbf{r}_D \in \mathbb{R}^{M_D}$ and $\mathbf{r}_N \in \mathbb{R}^{M_N}$ collect the Dirichlet and Neumann residuals at boundary collocation points. The corresponding discrete system has a block structure

$$\underbrace{\begin{bmatrix} \mathbf{A}_m^{(p)} & \mathbf{A}_m^{(\text{div})} & \mathbf{A}_m^{(\text{cur})} \\ \mathbf{A}_c^{(p)} & \mathbf{0} & \mathbf{A}_c^{(\text{cur})} \\ \mathbf{A}_D^{(p)} & \mathbf{0} & \mathbf{0} \\ \mathbf{0} & \mathbf{A}_N^{(\text{div})} & \mathbf{A}_N^{(\text{cur})} \end{bmatrix}}_{\mathbf{A}_{\text{flow}} \in \mathbb{R}^{M_{\text{tot}} \times N_\theta}} \begin{bmatrix} \boldsymbol{\theta}^{(p)} \\ \boldsymbol{\theta}^{(\text{div})} \\ \boldsymbol{\theta}^{(\text{cur})} \end{bmatrix} - \underbrace{\begin{bmatrix} \mathbf{b}_m \\ \mathbf{b}_c \\ \mathbf{b}_D \\ \mathbf{b}_N \end{bmatrix}}_{\mathbf{b}_{\text{flow}} \in \mathbb{R}^{M_{\text{tot}}}}, \quad M_{\text{tot}} = 2M_\Omega + M_D + M_N,$$

where each row of \mathbf{A}_m , \mathbf{A}_c , \mathbf{A}_D , \mathbf{A}_N is obtained by evaluating the bases and their derivatives at the corresponding collocation point and inserting them into the constitutive, continuity, and boundary residual definitions. Finally, the weighting matrix in (5) is diagonal under collocation

$$\mathbf{W} = \text{diag}(\mathbf{w}_m, \mathbf{w}_c, \mathbf{w}_D, \mathbf{w}_N) \in \mathbb{R}^{M_{\text{tot}} \times M_{\text{tot}}},$$

where \mathbf{w}_m collects $w_m(x_j)$ on interior points, \mathbf{w}_c collects $w_c(x_j)$ on interior points, and \mathbf{w}_D and \mathbf{w}_N collect $w_D(x_b)$ and $w_N(x_b)$ on Dirichlet and Neumann boundary points.

Supercritical CO₂ storage models

We consider a supercritical CO₂ storage benchmark in a square porous domain $\Omega = [0, 762] \text{ m} \times [0, 762] \text{ m}$ (Fig. 2a) under two permeability settings: (i) a homogeneous case with constant permeability $\kappa = 0.3 \text{ D}$, and (ii) a heterogeneous case in which $\kappa(\mathbf{x})$ is generated as a geologically realistic Gaussian random field. The heterogeneous permeability field is shown in Fig. 3a and has a permeability contrast of 502. A passive tracer is injected at the left boundary. Except for the permeability distribution, the rest of the setups of the two cases are identical.

Boundary conditions: on the left boundary ($x = 0$), we set constant pressure $p = 103.4 \text{ bar}$ and impose a passive tracer pulse with concentration $c_{\text{in}} = 100 \text{ ppm}$ lasted for the first 10 days. On the top boundary ($y = 762 \text{ m}$), we impose an outward mass-flux $q_y = 586 \text{ kg day}^{-1} \text{ m}^{-2}$. The right boundary ($x = 762 \text{ m}$) is no-flow ($q_x = 0$), and the bottom boundary ($y = 0$) is no-flow ($q_y = 0$).

Fluid and rock properties: rock and fluid properties are uniform unless otherwise stated by the permeability setting: porosity $\varepsilon = 0.25$, fluid viscosity $\mu = 0.04 \text{ cP}$, compressibility $c_f = 2.90 \times 10^{-3} \text{ bar}^{-1}$, and reference density $\rho_0 = 384 \text{ kg m}^{-3}$ at $50 \text{ }^\circ\text{C}$ and $p_0 = 103.4 \text{ bar}$.

Reference and discretizations: for the homogeneous case, we use an FVM solution computed on a 1000×1000 structured uniform mesh as the ground-truth, which provides a reliable numerical proxy for the true solution in this setting. For the heterogeneous case, a ground truth analogous to the homogeneous fine-grid proxy is not available by grid refinement, because the permeability is discretely-specified through a generated heterogeneous realization rather than a known true continuous field. For both the homogeneous and heterogeneous cases, the baseline FVM solutions uses a 50×50 structured uniform mesh. For NBM, we employ collocation on a 50×50 uniform interior grid (2500 interior points) to match the spatial resolution of the 50×50 FVM baseline discretization. We place 50 uniformly distributed collocation points on each boundary, yielding 2700 total collocation points. Vanilla PINN baselines using the same spatial resolution are provided in **SI.8**. For the comparison between using and not using the energy-consistent weight (4), the baseline is uniform weighting with constant weights of 1.

Manufactured-solution benchmark with separable multiscale permeability

To quantify intrinsic accuracy in a multiscale setting where grid refinement does not provide a ground-truth proxy, we introduce a manufactured-solution benchmark. We consider a simplified incompressible case with a spatially multiscale yet separable permeability field. We consider

$$\mathbf{u} = -\frac{\kappa(x, y)}{\mu} \nabla p, \quad \nabla \cdot \mathbf{u} = 0, \quad (x, y) \in \Omega,$$

posed on a regular domain Ω with constant viscosity μ . The permeability is constructed as a separable product $\kappa(x, y) = a(x)b(y)$, where a and b are oscillatory 1D fields to induce controlled heterogeneity and contrast while remaining smooth within each coordinate. Specifically, we use,

$$a(x) = \exp\left(s_x \frac{\varphi_x(x)}{\max |\varphi_x|}\right), \quad b(y) = \exp\left(s_y \frac{\varphi_y(y)}{\max |\varphi_y|}\right),$$

with $\varphi_x(x) = \beta_{x1} \sin(2\pi x) + \beta_{x2} \cos(4\pi x)$ and $\varphi_y(y) = \beta_{y1} \cos(2\pi y) + \beta_{y2} \sin(2\pi y)$. The scaling parameters $s_x = \frac{1}{2} \log(\mathcal{C}_x)$ and $s_y = \frac{1}{2} \log(\mathcal{C}_y)$ control the 1D contrasts \mathcal{C}_x and \mathcal{C}_y and thereby the overall contrast. All permeability values are evaluated on cell centers of a uniform grid. We thus can manufacture an exact pressure field by defining 1D antiderivatives of the reciprocal coefficients,

$$I_x(x) = \int_{x_{\min}}^x \frac{1}{a(s)} ds, \quad I_y(y) = \int_{y_{\min}}^y \frac{1}{b(s)} ds,$$

and setting $p(x, y) = p_0 + B(C_x I_x(x) + C_y I_y(y))$, where p_0 is a reference pressure, B sets the amplitude, and C_x, C_y specify the relative strengths of the x and y components. We thus have

$$\partial_x p = B \frac{C_x}{a(x)}, \quad \partial_y p = B \frac{C_y}{b(y)},$$

which implies an analytic velocity field

$$u_x(x, y) = -\frac{\kappa(x, y)}{\mu} \partial_x p = -\frac{B C_x}{\mu} b(y), \quad u_y(x, y) = -\frac{\kappa(x, y)}{\mu} \partial_y p = -\frac{B C_y}{\mu} a(x).$$

Since u_x depends only on y and u_y depends only on x , the divergence-free constraint holds identically. The corresponding boundary conditions for p are taken from the manufactured pressure, and the benchmark admits an exact solution pair (p, \mathbf{u}) for any chosen contrasts and coefficients. For implementation, the permeability factors $a(x)$ and $b(y)$ are evaluated on cell-center coordinates, giving $\kappa_{ij} = k_0 a(x_i) b(y_j)$ with a uniform scaling factor k_0 . The integrals I_x and I_y are computed on the 1D grids to assemble p_{ij} on cell centers, using either a cumulative trapezoidal rule on the uniform grid or a higher-accuracy piecewise Gauss–Legendre 8-point quadrature on each cell interval. The exact velocity is evaluated from the closed-form expressions implied by the manufactured construction, avoiding numerical differencing.

In the experiments of Fig. 3k–s, we set $\Omega = [-1, 1] \times [-1, 1]$ with $p_0 = 34$ bar, $\mu = 1.0$ cp, $B = -20$, and $(C_x, C_y) = (1.0, -0.6)$, and use $k_0 = 0.1$. The permeability contrasts of the 1D factors are prescribed as $C_x = \max(a)/\min(a) = 200$ and $C_y = \max(b)/\min(b) = 20$ under global normalization and mean preservation, yielding an overall contrast is about 1078, while varying (C_x, C_y) generates permeability fields with different contrast levels. This manufactured benchmark only provides exact pressure and velocity. The concentration ground-truth is obtained by solving the transport equation with an FVM discretization using first-order upwinding driven by the manufactured velocity field, since an exact closed-form concentration solution is generally difficult to construct for heterogeneous advection under general initial and boundary conditions.

Residual–error certificate for the weighted Darcy projection

We consider a single implicit time step of the slightly-compressible Darcy update $T^n \rightarrow T^{n+1}$. The density increment satisfies $\rho(p^{n+1}) - \rho(p^n) = \rho_0 c_f (p^{n+1} - p^n)$. For clarity, here we show linearization by lagging the density prefactor at time level n and introduce $\alpha := \rho(p^n) \frac{\kappa}{\mu}$, $\beta := \frac{\varepsilon \rho_0 c_f}{\Delta T}$. Let (p, \mathbf{q}) denote the exact mixed state and $(\tilde{p}, \tilde{\mathbf{q}})$ its NBM approximation. The corresponding errors are $e_p = \tilde{p} - p$ and $e_{\mathbf{q}} = \tilde{\mathbf{q}} - \mathbf{q}$. We write (M1)–(M2) in the linearized time step-dependent form

$$\mathbf{q} + a \nabla p = 0 \quad \text{in } \Omega, \tag{M11}$$

$$\nabla \cdot \mathbf{q} + \beta p = 0 \quad \text{in } \Omega, \tag{M12}$$

with mixed boundary conditions

$$p = p_D \quad \text{on } \partial\Omega_p, \quad \mathbf{q} \cdot \mathbf{n} = q_N \quad \text{on } \partial\Omega_q.$$

We define the residual components

$$\begin{aligned} r_m &:= \tilde{\mathbf{q}} + a \nabla \tilde{p}, \\ r_c &:= \nabla \cdot \tilde{\mathbf{q}} + \beta \tilde{p}, \\ r_D &:= \tilde{p} - p_D, \\ r_N &:= \tilde{\mathbf{q}} \cdot \mathbf{n} - q_N, \end{aligned}$$

and collect them in the weighted residual norm

$$\|R(\tilde{p}, \tilde{\mathbf{q}})\|_W^2 := \|w_m r_m\|_{L^2(\Omega)}^2 + \|w_c r_c\|_{L^2(\Omega)}^2 + \|w_D r_D\|_{L^2(\partial\Omega_p)}^2 + \|w_N r_N\|_{L^2(\partial\Omega_q)}^2,$$

where w_\star is given in (4) for $\star \in \{m, c, D, N\}$. We further write the natural graph norm of error

$$\|(e_p, e_{\mathbf{q}})\|_{\mathcal{E}}^2 := \|e_p\|_{H^1(\Omega)}^2 + \|e_{\mathbf{q}}\|_{H(\text{div}; \Omega)}^2 + \|e_p\|_{L^2(\partial\Omega_p)}^2 + \|e_{\mathbf{q}}\|_{L^2(\partial\Omega_q)}^2.$$

The next lemma shows that this weighted residual norm is equivalent to the natural graph norm or error such that $\|R(\tilde{p}, \tilde{\mathbf{q}})\|_W \asymp \|(e_p, e_{\mathbf{q}})\|_{\mathcal{E}}$. Consequently, we provide a computable residual–error certificate.

Lemma 2 (Residual–error equivalence for the weighted first-order least-squares Darcy problem). *Assume $0 < a_{\min} \leq a(x) \leq a_{\max}$ and $0 < \beta_{\min} \leq \beta(x) \leq \beta_{\max}$ a.e. in Ω . Assume the boundary split $\partial\Omega = \partial\Omega_p \cup \partial\Omega_q$ ensures uniqueness, e.g., $|\partial\Omega_p| > 0$. Then there exist constants $C_1, C_2 > 0$, independent of $(\tilde{p}, \tilde{\mathbf{q}})$, such that*

$$C_1 \|(e_p, e_{\mathbf{q}})\|_{\mathcal{E}} \leq \|R(\tilde{p}, \tilde{\mathbf{q}})\|_W \leq C_2 \|(e_p, e_{\mathbf{q}})\|_{\mathcal{E}}, \quad (\text{M13})$$

Proof. The equivalence between $\|\cdot\|_W$ and the corresponding unweighted L^2 -residual norm follows from $0 < c_\star \leq w_\star \leq C_\star$. The error–residual equivalence (M13) is the U -ellipticity result for the first-order system least-squares operator associated with (M11)–(M12); see, e.g., [35, 54]. \square

Residual–error certificate for the stabilized transport projection

We consider a single implicit transport substep $t^m \rightarrow t^{m+1}$ based on the upwind control-volume balance in (6). Let c denote the exact concentration and let \tilde{c} be its NBM approximation, and define the error $e_c := \tilde{c} - c$ and the corresponding cell-wise time step-dependent residual $r_{\text{up}} := A_{\text{up}}\tilde{c} - b$, so that $r_{\text{up}} = A_{\text{up}}e_c$. For an arbitrary cellwise scalar field $v = \{v_K\}$, define the pore-volume–scaled diagonal mass weight

$$D := \text{diag}(\varepsilon|K|), \quad \|v\|_D^2 := \sum_K (\varepsilon|K|) v_K^2,$$

and the upwind dissipation semi-norm over interior faces as follows. For each interior face $f = K|L$, let $\mathbf{n}_{K,f}$ be the unit normal on f pointing outward from cell K , and set $\alpha_f := |(\mathbf{u} \cdot \mathbf{n}_{K,f})_f| |f|$. Then

$$|v|_{\text{up}}^2 := \frac{1}{2} \sum_{f=K|L} \alpha_f (v_K - v_L)^2.$$

We then define the transport energy norm

$$\|v\|_{\mathcal{E}, \text{tr}}^2 := \frac{1}{\Delta t} \|v\|_D^2 + |v|_{\text{up}}^2.$$

Since $|v|_{\text{up}}^2 \geq 0$, the transport energy norm of error controls the cellwise Euclidean error of concentration

$$\|e_c\|_2 \leq \sqrt{\frac{\Delta t}{\varepsilon|K|_{\min}}} \|e_c\|_{\mathcal{E}, \text{tr}}, \quad |K|_{\min} := \min_K |K|. \quad (\text{T.3a})$$

On a fixed discretization, $\|\cdot\|_{\mathcal{E}, \text{tr}}$ and $\|\cdot\|_2$ are equivalent up to constants. The next lemma shows that the Euclidean residual norm $\|r_{\text{up}}\|_2$ is equivalent to the transport energy norm of the error, i.e., $\|r_{\text{up}}\|_2 \asymp \|e_c\|_{\mathcal{E}, \text{tr}}$, thereby providing a computable residual–error certificate.

Lemma 3 (Residual–error equivalence for upwind control-volume transport problem). *Assume $\varepsilon > 0$ and a fixed transport discretization (mesh, velocity field, and time step). Then there exist constants $C_1, C_2 > 0$, independent of \tilde{c} , such that*

$$C_1 \|e_c\|_{\mathcal{E},\text{tr}} \leq \|r_{\text{up}}\|_2 \leq C_2 \|e_c\|_{\mathcal{E},\text{tr}}. \quad (\text{M14})$$

Proof. For the upwind control-volume operator $A = \frac{1}{\Delta t}D + V$, the symmetric part $V_s = \frac{1}{2}(V + V^\top)$ induces the classical upwind jump dissipation, i.e., $v^\top V_s v = |v|_{\text{up}}^2 \geq 0$ for all cell vectors v ; see, e.g., [55, 56]. Hence $G := \frac{1}{\Delta t}D + V_s \succ 0$ and $\|v\|_{\mathcal{E},\text{tr}}^2 = v^\top G v$. Writing $A = G + V_k$ with skew-symmetric $T_k = \frac{1}{2}(V - V^\top)$, the DPG theory yields the residual–error equivalence in the induced dual norm, $\|e\|_G \asymp \|Ae\|_{G^{-1}}$; see, e.g., [37, 38, 57]. Finally, on a fixed discretization, the Euclidean residual $\|r\|_2$ is equivalent to $\|r\|_{G^{-1}}$ by standard spectral norm equivalence for symmetric positive definite matrices, which completes (M14). \square

NBM–OL implementation

NBM–OL implementation is very structured as shown in Fig. 4. Below, we show a complete yet high-level description with the optional POD compression included (specific configurations are provide in **SI.11**). We begin by outlining the shared aspects of the learning pipeline used in the three experiments:

- Case-I: permeability-varying Darcy flow operator;
- Case-II: boundary-flux-varying Darcy flow operator;
- Case-III: boundary-flux/concentration-varying Darcy–transport operator.

Across all cases, NBM–OL learns a map from a parameterization (and time, when applicable) to the solution coefficients in the neural basis space, enabling rapid inference of pressure, flux/velocity, and concentration fields for new parameter instances.

Common workflow. Given a parameter input ξ (and time t when relevant), the overall procedure is as follows. When POD compression is not used, steps (ii) and (iii) are omitted.

- (i) define a parametrization of the operator family;
- (ii) generate solution coefficient snapshots by solving sampled training instances using NBM;
- (iii) compress the solution coefficient snapshots with POD to define a latent coordinate \mathbf{z} ;
- (iv) train an MLP operator \mathcal{F} to predict \mathbf{z} using a self-supervised objective based on residual \mathcal{E}_{rel} ;
- (v) at inference, evaluate \mathcal{F} to obtain \mathbf{z} , reconstruct full solution coefficients via POD projection, and recover fields at collocation locations by evaluating the neural basis expansion. When needed, the velocity field is obtained from the reconstructed mass flux and density.

Case-I: permeability-varying Darcy flow operator. We parametrize permeability heterogeneity using a piecewise-constant 5×5 blockwise field (block25). Each block25 realization is generated from a Gaussian random field model (**SI**), controlled by the heterogeneity level, correlation length(s), and a rotation angle orienting the principal correlation direction. Given a sampled block25 instance, we apply it to the base permeability template $\kappa_{\text{ref}}(\mathbf{x})$ via blockwise multiplication to obtain $\kappa(\mathbf{x}; \xi_\kappa)$. For each training sample, NBM produces steady coefficient snapshots (θ_p, θ_u) ;

we apply POD to $\boldsymbol{\theta}_p$ and $\boldsymbol{\theta}_u$ separately and define $\mathbf{z} = [\mathbf{z}_p; \mathbf{z}_u]$. We learn the mapping $\mathcal{F}(\boldsymbol{\xi}_\kappa) \mapsto \mathbf{z}$ using a two-branch multilayer perceptron (MLP), with one branch predicting \mathbf{z}_p and the other predicting \mathbf{z}_u , trained via a residual-based objective obtained by evaluating the Darcy flow NBM residual in the reduced coordinate system. At inference, we reconstruct the steady pressure and velocity fields from the coefficients predicted by the network.

Case-II: boundary-flux-varying Darcy flow operator. We parametrize the operator family by a scalar control g^{top} specifying the outward top-boundary mass-flux. For each sampled g_i^{top} , we run NBM to generate a coefficient trajectory over the Darcy time horizon, $\{\boldsymbol{\theta}(t^n; g_i^{\text{top}})\}$, where $\boldsymbol{\theta} = [\boldsymbol{\theta}_{\text{div}}; \boldsymbol{\theta}_{\text{curl}}; \boldsymbol{\theta}_p] \in \mathbb{R}^{3N_b}$ collects the structured Helmholtz components of mass-flux together with pressure. We apply POD to $\boldsymbol{\theta}_{\text{div}}$, $\boldsymbol{\theta}_{\text{curl}}$, and $\boldsymbol{\theta}_p$ separately to obtain $\mathbf{z} = [\mathbf{z}_{\text{div}}; \mathbf{z}_{\text{curl}}; \mathbf{z}_p]$. We learn a time-conditioned latent map $\mathbf{z}(t) = \mathcal{F}(g^{\text{top}}, t)$ using three MLP branches (one per latent block), trained by minimizing the Darcy flow NBM residual in the reduced coordinate system. At inference, for new g^{top} and t , we reconstruct $\boldsymbol{\theta}(t)$ and recover pressure and velocity fields at collocation locations.

Case-III: boundary-flux/concentration-varying Darcy–transport operator. We design a coupled Darcy–transport setting with two scalar controls: g^{top} (top-boundary outward mass-flux) and c^{left} (left-boundary injected tracer concentration). For each sampled pair $(g_i^{\text{top}}, c_i^{\text{left}})$, we directly use the pretrained Case-II model to infer the velocity sequence $\{\mathbf{u}^{n+1}(g_i^{\text{top}})\}$ at coarse Darcy time steps indexed by n . Each coarse Darcy step (ΔT) is split into N_{tr} transport substeps with $\Delta t = \Delta T/N_{\text{tr}}$, and NBM is used to generate concentration coefficient snapshots $\{\boldsymbol{\theta}_c(t^{m+1}; g_i^{\text{top}}, c_i^{\text{left}})\}$ over all substeps indexed by m . We apply POD to $\{\boldsymbol{\theta}_c\}$ to define a latent concentration state \mathbf{z}_c . We then learn a single time-conditioned latent map $\mathbf{z}_c(t) = \mathcal{F}(g^{\text{top}}, c^{\text{left}}, t)$, trained by minimizing the transport NBM residual expressed in latent form. At inference, we obtain the Darcy velocity sequence from the pretrained Case-II model, evaluate \mathcal{F} to reconstruct $\boldsymbol{\theta}_c(t)$, and recover concentration fields at collocation locations over the time horizon.

Data and Code Availability

The code and data used in this study are available in the GitHub repository <https://github.com/neural-basis-method/nbm>

References

- [1] Olav Møyner. Multiscale simulation of flow and transport in porous media. *Collections*, 52(08), 2019.
- [2] Eliyahu M Farber, Nicola M Seraphim, Keshava Tamakuwala, Andreas Stein, Maja Rücker, and David Eisenberg. Porous materials: The next frontier in energy technologies. *Science*, 390(6772):eadn9391, 2025.
- [3] Juan Alcalde, Stephanie Flude, Mark Wilkinson, Gareth Johnson, Katriona Edlmann, Clare E Bond, Vivian Scott, Stuart MV Gilfillan, Xènia Ogaya, and R Stuart Haszeldine. Estimating geological co2 storage security to deliver on climate mitigation. *Nature communications*, 9(1):2201, 2018.
- [4] Samuel Krevor, Heleen De Coninck, Sarah E Gasda, Navraj Singh Ghaleigh, Vincent de Gooyert, Hadi Hajibeygi, Ruben Juanes, Jerome Neufeld, Jennifer J Roberts, and Floris Swennen-

- huis. Subsurface carbon dioxide and hydrogen storage for a sustainable energy future. *Nature Reviews Earth & Environment*, 4(2):102–118, 2023.
- [5] Allen G Hunt and Muhammad Sahimi. Flow, transport, and reaction in porous media: Percolation scaling, critical-path analysis, and effective medium approximation. *Reviews of Geophysics*, 55(4):993–1078, 2017.
- [6] Eric Vanden-Eijnden. Heterogeneous multiscale methods: a review. *Communications in Computational Physics* 2 (3), pages 367–450, 2007.
- [7] George Em Karniadakis, Ioannis G Kevrekidis, Lu Lu, Paris Perdikaris, Sifan Wang, and Liu Yang. Physics-informed machine learning. *Nature Reviews Physics*, 3(6):422–440, 2021.
- [8] Maziar Raissi, Paris Perdikaris, and George E Karniadakis. Physics-informed neural networks: A deep learning framework for solving forward and inverse problems involving nonlinear partial differential equations. *Journal of Computational physics*, 378:686–707, 2019.
- [9] Sifan Wang, Shyam Sankaran, Hanwen Wang, and Paris Perdikaris. An expert’s guide to training physics-informed neural networks (2023). *Preprint at <https://arxiv.org/pdf/2308.08468.pdf>*, 2023.
- [10] Sifan Wang, Yujun Teng, and Paris Perdikaris. Understanding and mitigating gradient flow pathologies in physics-informed neural networks. *SIAM Journal on Scientific Computing*, 43(5):A3055–A3081, 2021.
- [11] Rafael Bischof and Michael A Kraus. Multi-objective loss balancing for physics-informed deep learning. *Computer Methods in Applied Mechanics and Engineering*, 439:117914, 2025.
- [12] Aditi Krishnapriyan, Amir Gholami, Shandian Zhe, Robert Kirby, and Michael W Mahoney. Characterizing possible failure modes in physics-informed neural networks. *Advances in neural information processing systems*, 34:26548–26560, 2021.
- [13] Chenxi Wu, Min Zhu, Qinyang Tan, Yadhu Kartha, and Lu Lu. A comprehensive study of non-adaptive and residual-based adaptive sampling for physics-informed neural networks. *Computer Methods in Applied Mechanics and Engineering*, 403:115671, 2023.
- [14] Sifan Wang, Xinling Yu, and Paris Perdikaris. When and why pinns fail to train: A neural tangent kernel perspective. *Journal of Computational Physics*, 449:110768, 2022.
- [15] Zhihang Xu, Min Wang, and Zhu Wang. Weak transnet: A petrov-galerkin based neural network method for solving elliptic pdes. *arXiv preprint [arXiv:2506.14812](https://arxiv.org/abs/2506.14812)*, 2025.
- [16] Susanne C Brenner and L Ridgway Scott. *The mathematical theory of finite element methods*. Springer, 2008.
- [17] Ivo Babuška and Werner C Rheinboldt. A-posteriori error estimates for the finite element method. *International journal for numerical methods in engineering*, 12(10):1597–1615, 1978.
- [18] George Cybenko. Approximation by superpositions of a sigmoidal function. *Mathematics of control, signals and systems*, 2(4):303–314, 1989.
- [19] Andrew R Barron. Universal approximation bounds for superpositions of a sigmoidal function. *IEEE Transactions on Information theory*, 39(3):930–945, 2002.

- [20] Dmitry Yarotsky. Error bounds for approximations with deep relu networks. *Neural networks*, 94:103–114, 2017.
- [21] Guang-Bin Huang, Qin-Yu Zhu, and Chee-Kheong Siew. Extreme learning machine: theory and applications. *Neurocomputing*, 70(1-3):489–501, 2006.
- [22] Jingrun Chen, Xurong Chi, Zhouwang Yang, et al. Bridging traditional and machine learning-based algorithms for solving pdes: the random feature method. *J Mach Learn*, 1(3):268–298, 2022.
- [23] Ali Rahimi and Benjamin Recht. Random features for large-scale kernel machines. *Advances in neural information processing systems*, 20, 2007.
- [24] Suchuan Dong and Zongwei Li. Local extreme learning machines and domain decomposition for solving linear and nonlinear partial differential equations. *Computer Methods in Applied Mechanics and Engineering*, 387:114129, 2021.
- [25] Zezhong Zhang, Feng Bao, Lili Ju, and Guannan Zhang. Transferable neural networks for partial differential equations. *Journal of Scientific Computing*, 99(1):2, 2024.
- [26] Xiaojun Chen, Robert S Womersley, and Jane J Ye. Minimizing the condition number of a gram matrix. *SIAM Journal on optimization*, 21(1):127–148, 2011.
- [27] Shijun Zhang, Hongkai Zhao, Yimin Zhong, and Haomin Zhou. Fourier multi-component and multi-layer neural networks: Unlocking high-frequency potential. *arXiv preprint arXiv:2502.18959*, 2025.
- [28] Jan Willem van Beek, Victorita Dolean, and Ben Moseley. Local feature filtering for scalable and well-conditioned domain-decomposed random feature methods. *Computer Methods in Applied Mechanics and Engineering*, 449:118583, 2026.
- [29] Jingrun Chen and Longze Tan. High-precision randomized iterative methods for the random feature method. *arXiv preprint arXiv:2409.15818*, 2024.
- [30] Xinwei Hu, Jingrun Chen, and Haijun Yu. A morphology-adaptive random feature method for inverse source problem of the helmholtz equation. *arXiv preprint arXiv:2510.09213*, 2025.
- [31] Shijun Zhang, Hongkai Zhao, Yimin Zhong, and Haomin Zhou. Why shallow networks struggle to approximate and learn high frequencies. *Information and Inference: A Journal of the IMA*, 14(3):iaaf022, 2025.
- [32] Xurong Chi, Jingrun Chen, and Zhouwang Yang. The random feature method for solving interface problems. *Computer Methods in Applied Mechanics and Engineering*, 420:116719, 2024.
- [33] P.B. Bochev and M.D. Gunzburger. *Least-Squares Finite Element Methods*. Applied Mathematical Sciences. Springer New York, 2009.
- [34] Gerhard Starke. Multilevel boundary functionals for least-squares mixed finite element methods. *SIAM journal on numerical analysis*, 36(4):1065–1077, 1999.
- [35] Zhiqiang Cai, R Lazarov, Thomas A Manteuffel, and Stephen F McCormick. First-order system least squares for second-order partial differential equations: Part i. *SIAM Journal on Numerical Analysis*, 31(6):1785–1799, 1994.

- [36] Zhiqiang Cai, Thomas A Manteuffel, and Stephen F McCormick. First-order system least squares for second-order partial differential equations: Part ii. *SIAM Journal on Numerical Analysis*, 34(2):425–454, 1997.
- [37] Leszek Demkowicz and Jayadeep Gopalakrishnan. A class of discontinuous petrov–galerkin methods. part i: The transport equation. *Computer Methods in Applied Mechanics and Engineering*, 199(23-24):1558–1572, 2010.
- [38] Leszek Demkowicz and Jay Gopalakrishnan. A class of discontinuous petrov–galerkin methods. ii. optimal test functions. *Numerical Methods for Partial Differential Equations*, 27(1):70–105, 2011.
- [39] Lu Lu, Pengzhan Jin, Guofei Pang, Zhongqiang Zhang, and George Em Karniadakis. Learning nonlinear operators via deepnet based on the universal approximation theorem of operators. *Nature machine intelligence*, 3(3):218–229, 2021.
- [40] Sifan Wang, Hanwen Wang, and Paris Perdikaris. Learning the solution operator of parametric partial differential equations with physics-informed deepnets. *Science advances*, 7(40):eabi8605, 2021.
- [41] Nikola Kovachki, Zongyi Li, Burigede Liu, Kamyar Azizzadenesheli, Kaushik Bhattacharya, Andrew Stuart, and Anima Anandkumar. Neural operator: Learning maps between function spaces with applications to pdes. *Journal of Machine Learning Research*, 24(89):1–97, 2023.
- [42] Martin A Grepl and Anthony T Patera. A posteriori error bounds for reduced-basis approximations of parametrized parabolic partial differential equations. *ESAIM: Mathematical Modelling and Numerical Analysis*, 39(1):157–181, 2005.
- [43] Yuan Qiu, Wolfgang Dahmen, and Peng Chen. Variationally correct operator learning: Reduced basis neural operator with a posteriori error estimation. *arXiv preprint arXiv:2512.21319*, 2025.
- [44] Leszek Demkowicz, Jay Gopalakrishnan, and Antti H Niemi. A class of discontinuous petrov–galerkin methods. part iii: Adaptivity. *Applied numerical mathematics*, 62(4):396–427, 2012.
- [45] Kaiming He, Xiangyu Zhang, Shaoqing Ren, and Jian Sun. Deep residual learning for image recognition. In *Proceedings of the IEEE conference on computer vision and pattern recognition*, pages 770–778, 2016.
- [46] James C Robinson, José L Rodrigo, and Witold Sadowski. *The three-dimensional Navier–Stokes equations: Classical theory*, volume 157. Cambridge university press, 2016.
- [47] Junping Wang, Yanqiu Wang, and Xiu Ye. A robust numerical method for stokes equations based on divergence-free h (div) finite element methods. *SIAM Journal on Scientific Computing*, 31(4):2784–2802, 2009.
- [48] Alfio Quarteroni, Andrea Manzoni, and Federico Negri. *Reduced basis methods for partial differential equations: an introduction*, volume 92. Springer, 2015.
- [49] GR Gavalas, PC Shah, and John H Seinfeld. Reservoir history matching by bayesian estimation. *Society of Petroleum Engineers Journal*, 16(06):337–350, 1976.

- [50] Dean S Oliver and Yan Chen. Recent progress on reservoir history matching: a review. *Computational Geosciences*, 15(1):185–221, 2011.
- [51] David Gottlieb and Chi-Wang Shu. On the gibbs phenomenon and its resolution. *SIAM review*, 39(4):644–668, 1997.
- [52] Anthony T Patera. A spectral element method for fluid dynamics: laminar flow in a channel expansion. *Journal of computational Physics*, 54(3):468–488, 1984.
- [53] Zezhong Zhang, Feng Bao, Lili Ju, and Guannan Zhang. Transnet: Transferable neural networks for partial differential equations. *arXiv preprint arXiv:2301.11701*, 2023.
- [54] Gregor Gantner and Rob Stevenson. Further results on a space-time fosl formulation of parabolic pdes. *ESAIM: Mathematical Modelling and Numerical Analysis*, 55(1):283–299, 2021.
- [55] Franck Boyer. Analysis of the upwind finite volume method for general initial-and boundary-value transport problems. *IMA Journal of Numerical Analysis*, 32(4):1404–1439, 2012.
- [56] Timothy Barth, Raphaële Herbin, and Mario Ohlberger. *Finite Volume Methods: Foundation and Analysis*, pages 1–60. John Wiley & Sons, Ltd, 2017.
- [57] Leszek Demkowicz and Jay Gopalakrishnan. The discontinuous petrov–galerkin method. *Acta Numerica*, 34:293–384, 2025.

Supplementary information

1 Finite-volume approximation of Darcy flow–transport system

For reference solutions, we solve the coupled Darcy flow–transport system using finite-volume method on structured and uniform Cartesian grids. Because the transported scalar is passive and does not influence the flow, the system is solved sequentially: the Darcy flow problem (M1)–(M2) is first advanced in time, after which the transport equation (M3) is solved using the computed velocity field for each Darcy flow update period.

Darcy flow solution. We discretize (M1)–(M2) with a cell-centered finite-volume scheme using two-point flux approximation. We store pressure at cell centers and evaluate mass fluxes on cell faces from local pressure differences. For a face shared by two neighboring cells, we compute the normal mass flux by harmonic averaging the permeability and arithmetic averaging the density, which yields a locally conservative flux. After obtaining the pressure solution, we reconstruct the Darcy velocity from the conservative face mass-fluxes using the same fluxes defined by the finite-volume discretization, so the velocity is consistent with discrete conservation. Fluid density follows a standard slightly compressible equation of state. We handle the resulting nonlinearity with Picard iterations at each time step and update the density from the previous pressure iterate. We perform time integration with backward Euler, yielding an unconditionally stable implicit scheme. At each Picard iteration, we solve the resulting sparse linear system using BICGSTAB.

Transport solution. Given the Darcy velocity at the end of each Darcy update period, we solve (M3) using cell-centered finite-volume with first-order upwind fluxes for this pure advection. This choice ensures numerical stability and monotonicity for sharp concentration fronts. We choose to use backward Euler for time integration. To better resolve the concentration evolution, we advance the transport equation with a smaller time step than the Darcy flow solver. Within each Darcy update period, we hold the velocity field fixed at its terminal value and perform multiple transport substeps. This sequential strategy is consistent with the passive nature of the transport. The finite-volume update with upwind face fluxes preserves local conservation of the scalar at each transport substep.

2 Neural basis generation and evaluation

In NBM, we represent the solution field using a set of neural basis functions generated by a fixed-parameter multilayer residual network. In this section, we provide the general neural basis construction, including parameter initialization, domain scaling, and the evaluation of basis functions and their first- and second-order derivatives used to assemble the least-squares residual operators.

Neural basis definition. We evaluate the neural basis at M prescribed spatial points (e.g., collocation or quadrature points) in a d -dimensional domain. These points are collected row-wise in the matrix $X \in \mathbb{R}^{M \times d}$, where each row contains the spatial coordinates of one evaluation point. We construct the neural basis by applying a fixed-parameter residual network to the coordinates in X . We consider a network consist of L layers with widths $\{p_1, \dots, p_L\}$, and we set $p_0 = d$. For $\ell = 0, 1, \dots, L$, we denote by $A_\ell(X) \in \mathbb{R}^{M \times p_\ell}$ the matrix of layer- ℓ neural basis values evaluated at the spatial points in X , where rows correspond to spatial points and columns correspond to basis

functions. For each layer $\ell = 1, \dots, L$, we compute $A_\ell(X)$ from $A_{\ell-1}(X)$ via

$$\begin{aligned} t_\ell(X) &= A_{\ell-1}(X) W_\ell^T + \mathbf{1} b_\ell^T, \\ a_\ell(X) &= t_\ell(X) \odot \alpha_\ell^T, \\ z_\ell(X) &= \sigma(a_\ell(X)), \\ s_\ell(X) &= \beta_\ell A_{\ell-1}(X) P_\ell^T, \\ A_\ell(X) &= s_\ell(X) + z_\ell(X), \end{aligned}$$

where $W_\ell, P_\ell \in \mathbb{R}^{p_\ell \times p_{\ell-1}}$ are weight matrices, $b_\ell \in \mathbb{R}^{p_\ell}$ is a bias vector, $\alpha_\ell \in \mathbb{R}^{p_\ell}$ is a per-neuron shape factor, and $\beta_\ell \in \mathbb{R}$ is a residual-strength scalar. Here $\mathbf{1} \in \mathbb{R}^M$ denotes a vector of ones, and \odot denotes elementwise multiplication with broadcasting across spatial points. The activation $\sigma(\cdot)$, such as `tanh` acts elementwise; for each supported activation, we implement analytic expressions for σ' and σ'' . We take the columns of $A_L(X)$ as the neural basis functions evaluated at the M spatial points. Optionally, we form an extended basis by concatenating the outputs of selected intermediate layers with $A_L(X)$.

Layer concatenation and constant basis. In NBM, the neural basis is not restricted to the output of a single layer. Instead, we allow the basis to be formed by combining the outputs of multiple layers in the residual network. Let $\mathcal{I} = \{i_1, \dots, i_K\}$ be a user-specified index set with $0 \leq i_k \leq L$. We construct the neural basis evaluation matrix as

$$\Phi(X) = [A_{i_1}(X) \ A_{i_2}(X) \ \dots \ A_{i_K}(X)] \in \mathbb{R}^{M \times P}, \quad P = \sum_{k=1}^K p_{i_k},$$

where $A_{i_k}(X) \in \mathbb{R}^{M \times p_{i_k}}$ denotes the layer- i_k output evaluated at the M spatial points in X , as defined previously. Concatenating multiple layers allows the neural basis to simultaneously capture features at different levels of abstraction, which can be beneficial for deep networks where intermediate layers may encode physically meaningful structures. Optionally, we augment the neural basis with a constant function by appending a column of ones to $\Phi(X)$. This constant basis ensures that spatially uniform components can be represented explicitly in the solution expansion and improves robustness when enforcing PDE constraints that admit constant or near-constant null-space modes. The corresponding first- and second-order spatial derivatives of the constant basis are identically zero.

Analytic derivatives for PDE operators. To assemble PDE operators, we need to evaluate derivatives. Here, we consider the first- and second-order spatial derivatives. For each layer $\ell = 0, \dots, L$, we denote the Jacobian and Hessian of the layer- ℓ basis by

$$J_\ell(X) \in \mathbb{R}^{M \times p_\ell \times d}, \quad H_\ell(X) \in \mathbb{R}^{M \times p_\ell \times d \times d},$$

where $m = 1, \dots, M$ indexes the spatial points in X , $J_\ell(X)_{m, :, i}$ contains the partial derivatives $\partial A_\ell(x_m) / \partial x_i$, and $H_\ell(X)_{m, :, i, j}$ contains $\partial^2 A_\ell(x_m) / \partial x_i \partial x_j$. We compute $J_\ell(X)$ and $H_\ell(X)$ analytically by propagating derivatives through the residual mapping defined above. For each layer, the nonlinear branch $z_\ell(X) = \sigma(a_\ell(X))$ is differentiated using analytic expressions for σ' and σ'' , with the per-neuron shape factors explicitly included:

$$\frac{\partial z_\ell}{\partial t_\ell} = \sigma'(a_\ell) \odot \alpha_\ell^T, \quad \frac{\partial^2 z_\ell}{\partial t_\ell^2} = \sigma''(a_\ell) \odot (\alpha_\ell^2)^T,$$

where all operations act elementwise and are evaluated at the spatial points in X . In the first layer, the skip branch $s_1(X) = \beta_1 A_0(X) P_1^T$ contributes a constant Jacobian $\beta_1 P_1$ and a zero Hessian, while the nonlinear branch contributes via the chain rule applied to $t_1(X) = A_0(X) W_1^T + \mathbf{1} b_1^T$. For deeper layers ($\ell \geq 2$), we propagate $J_{\ell-1}(X)$ and $H_{\ell-1}(X)$ through the linear maps W_ℓ and P_ℓ , and add the standard second-order term arising from the composition of the nonlinearity with the affine mapping, which is proportional to $(\nabla t_\ell) \otimes (\nabla t_\ell)$. This analytic derivative evaluation enables the direct assembly of gradients, divergences, and Laplacians of the NBM solution representation at the spatial points in X , without numerical differentiation or automatic differentiation.

Neural basis initialization. We construct the fixed neural basis by explicitly initializing the parameters $\{W_\ell, b_\ell, P_\ell\}_{\ell=1}^L$ according to deterministic rules. For layers $\ell \geq 2$, the weight matrix $W_\ell \in \mathbb{R}^{p_\ell \times p_{\ell-1}}$ is initialized by independent standard normal samples, i.e., each entry is drawn from $\mathcal{N}(0, 1)$. The corresponding bias vector $b_\ell \in \mathbb{R}^{p_\ell}$ is sampled independently from a uniform distribution on $[-r, r]$, where r is a prescribed radius parameter. The residual projection matrix $P_\ell \in \mathbb{R}^{p_\ell \times p_{\ell-1}}$ is initialized as the identity matrix when $p_\ell = p_{\ell-1}$, and otherwise by zero mean Gaussian sampling with variance scaled as $1/\sqrt{p_{\ell-1}}$. Each neuron in the first layer defines an affine function $w^T x + b$, whose zero level set $w^T x + b = 0$ corresponds to a hyperplane in the physical domain. In two spatial dimensions, these hyperplanes reduce to straight lines. A naive random initialization of (w, b) may therefore generate multiple nearly coincident or strongly correlated hyperplanes, which can lead to an ill-conditioned neural basis. To mitigate this effect, we can apply some geometric filtering procedures to the first-layer parameters. Candidate neurons are generated by sampling unit normals w and offsets b , and are accepted only if they satisfy certain geometric diversity criteria. In two dimensions, we consider the normalized square domain $[-1, 1]^2$ and require that (i) the intersection chord length of the corresponding line with the square is not negligible relative to a reference length, and (ii) the line is not nearly parallel to, nor spatially clustered with, previously accepted lines. This filtering suppresses highly correlated first-layer basis functions without altering the network architecture or the subsequent layers.

First-layer scaling. The neural basis functions need to be evaluated on a physical spatial domain $\Omega = [x_1, \bar{x}_1] \times \cdots \times [x_d, \bar{x}_d] \subset \mathbb{R}^d$. For convenience, the first-layer basis functions are constructed and interpreted with respect to a normalized reference domain centered at the origin. Specifically, the first-layer neurons (e.g., hyperplanes $w^T x + b = 0$) and any associated geometric filtering are defined on the standard domain $[-1, 1]^d$. To make the first-layer basis independent of the absolute size and location of the physical domain, we apply an explicit affine rescaling that maps Ω to the normalized reference domain $[-1, 1]^d$. For each spatial dimension $i = 1, \dots, d$, we define the half-length and center

$$s_i = \frac{\bar{x}_i - x_i}{2}, \quad c_i = \frac{\bar{x}_i + x_i}{2},$$

so that the normalized coordinate is given by

$$\hat{x}_i = \frac{x_i - c_i}{s_i} \in [-1, 1].$$

Rather than rescaling the input coordinates explicitly, we absorb this affine transformation into the first-layer parameters. Let $W_{1,0}$, $P_{1,0}$, and $b_{1,0}$ denote the unscaled first-layer parameters defined on the normalized domain. The scaled parameters used in evaluation are

$$W_1 = W_{1,0} \text{diag}(s)^{-1}, \quad P_1 = P_{1,0} \text{diag}(s)^{-1}, \quad b_1 = b_{1,0} - W_{1,0} (c \oslash s),$$

where \oslash denotes elementwise division. Because the residual (skip) branch is linear in the input coordinates, this rescaling introduces an additional constant shift. We compensate for this shift

explicitly and evaluate the first-layer skip output as

$$s_1(X) = \beta_1 (X P_1^T) + \mathbf{1} \gamma_1^T, \quad \gamma_1 = -\beta_1 P_{1,0} (c \odot s).$$

Throughout this work, we consider axis-aligned rectangular domains, for which an affine mapping to the reference domain $[-1, 1]^d$ is exact and invertible. This construction guarantees that the shape, orientation, and spacing of the first-layer neural basis functions are defined consistently on the normalized reference domain $[-1, 1]^d$. All deeper layers ($\ell \geq 2$) operate only on the outputs of the first layer and therefore require no additional domain-dependent scaling.

3 Neural basis expressivity and stability

Here we show how a given neural basis space performs in representing target solution fields, pressure $p(\mathbf{x})$, concentration $c(\mathbf{x})$, and mass-flux $\mathbf{q}(\mathbf{x})$. As a representative test, we use the multiscale supercritical CO₂ storage problem in Fig. 3a. We take the respective solution snapshots at day 10 as the references.

Least-squares projection and best-approximation error. We measure neural basis expressivity by the smallest discrete relative L_2 error attainable when approximating the FVM reference fields. Concretely, for any target scalar field $s(\mathbf{x})$ (pressure, concentration, or dimensional components of mass-flux) sampled at M collocation points, we form the basis evaluation matrix $\Phi \in \mathbb{R}^{M \times N_b}$ with $\Phi_{ji} = \phi_i(\mathbf{x}_j)$ and solve the least-squares projection

$$\boldsymbol{\theta}^* = \arg \min_{\boldsymbol{\theta} \in \mathbb{R}^{N_b}} \|\Phi \boldsymbol{\theta} - \mathbf{s}\|_2^2, \quad \widehat{s}(\mathbf{x}) = \sum_{i=1}^{N_b} \theta_i^* \phi_i(\mathbf{x}), \quad (\text{S1})$$

where $\mathbf{s}_{\text{ref}} \in \mathbb{R}^M$ collects the reference values $s_{\text{ref}}(\mathbf{x}_j)$. The resulting $\|\widehat{s} - s_{\text{ref}}\|_2 / \|s_{\text{ref}}\|_2$ is therefore the minimum discrete relative L_2 error achievable by using this basis for approximating s_{ref} under the chosen sampling and norm. Pressure p and concentration c are treated directly as scalar targets in (S1). For the mass-flux $\mathbf{q} = (q_x, q_y)$, we evaluate expressivity componentwise by applying the same least-squares projection to the relevant scalar components. Specifically, we project q_x and q_y directly when no decomposition is used. When the Helmholtz decomposition is used, we first decompose the reference mass-flux into divergence-free and curl-free parts, $\mathbf{q}_{\text{ref}} = \mathbf{q}_{\text{ref}}^{(\text{div})} + \mathbf{q}_{\text{ref}}^{(\text{curl})}$, and then solve four scalar least-squares projections for $q_{x,\text{ref}}^{(\text{div})}, q_{y,\text{ref}}^{(\text{div})}, q_{x,\text{ref}}^{(\text{curl})}, q_{y,\text{ref}}^{(\text{curl})}$, using the corresponding neural vector-basis evaluation matrices for each subspace. The projected components are denoted by $\widehat{q}_x^{(\text{div})}, \widehat{q}_y^{(\text{div})}, \widehat{q}_x^{(\text{curl})}, \widehat{q}_y^{(\text{curl})}$, and we reconstruct the projected flux by

$$\widehat{q}_x = \widehat{q}_x^{(\text{div})} + \widehat{q}_x^{(\text{curl})}, \quad \widehat{q}_y = \widehat{q}_y^{(\text{div})} + \widehat{q}_y^{(\text{curl})}, \quad \widehat{\mathbf{q}} = (\widehat{q}_x, \widehat{q}_y).$$

We then report relative L_2 projection errors for q_x , q_y , and $|\mathbf{q}|$. Finally, we report the condition numbers of the corresponding least-squares operators, which characterize numerical stability of the projection.

Pressure projection: dual-layer versus single-layer basis. Pressure is smooth and dominated by low-frequency content, so both scalar bases approximate the reference field with very small projection error. The FVM reference pressure p_{ref} appears in Fig. S1a, and the absolute projection errors $|\widehat{p} - p_{\text{ref}}|$ for the dual-layer and single-layer bases appear in Fig. S1b–c. The relative L_2 projection errors and the corresponding condition numbers are summarized in Fig. S1d. Moving

from the dual-layer to the single-layer basis increases the best-approximation error from 0.001% to 0.0011%, a 10% increase in the minimum achievable relative L_2 error. Moving from the dual-layer to the single-layer basis increases the condition number from 2.6×10^8 to 1.7×10^{15} , an increase of about 7 orders of magnitude. The main difference is therefore not approximation quality but numerical conditioning. In the PDE-constrained least-squares projection, this level of ill-conditioning amplifies numerical noise in the solves and can destabilize the solution coefficient updates.

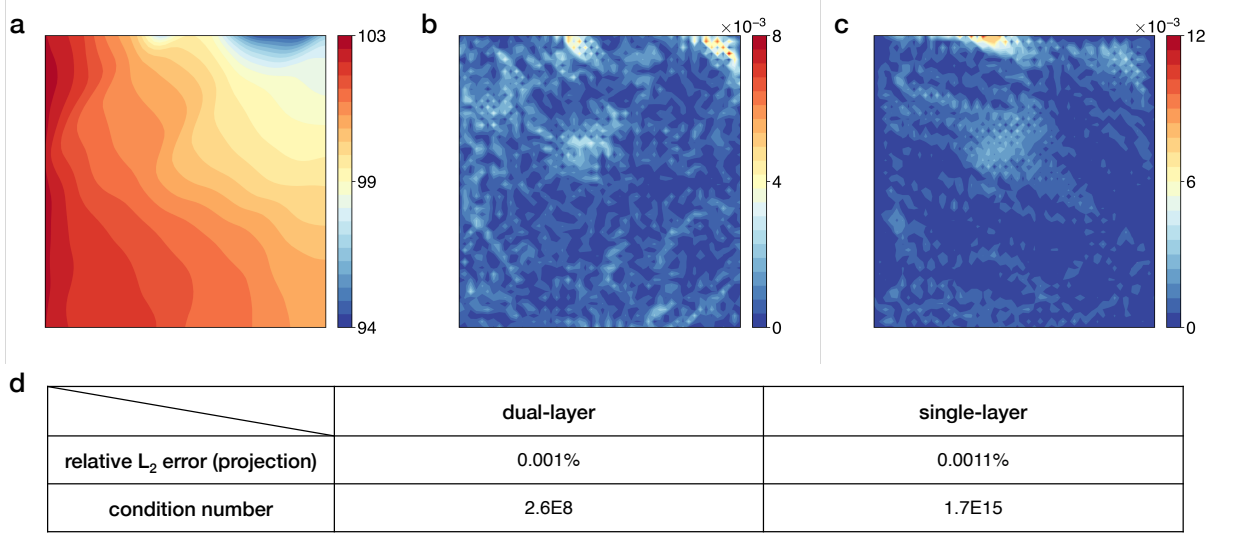


Fig. S1 | Neural basis expressivity and stability for pressure. **a**, FVM reference pressure p (bar). **b-c**, Absolute projection error using dual-layer and single-layer scalar neural basis, respectively **d**, Relative L_2 projection error and condition number of the projection system. **Note:** Pressure is reported in bar.

Mass-flux projection: dual-layer versus single-layer bases, with and without Helmholtz split. The mass-flux projection reveals two effects that matter in practice. A Helmholtz split improves best-approximation, and the single-layer construction can severely degrade conditioning. The reference magnitude $|\mathbf{q}_{\text{ref}}|$ and the component-wise absolute projection errors for q_x and q_y appear in Fig. S2a–e, and the relative L_2 errors together with condition numbers appear in Fig. S2f. Within each basis generator, adding the Helmholtz split reduces the best-approximation error. For the dual-layer basis, the errors decrease as

$$q_x : 1.00\% \rightarrow 0.86\% (-14\%), \quad q_y : 1.66\% \rightarrow 1.21\% (-27\%), \quad |\mathbf{q}| : 1.10\% \rightarrow 0.80\% (-27\%).$$

For the single-layer basis, the errors decrease as

$$q_x : 1.29\% \rightarrow 1.01\% (-22\%), \quad q_y : 1.92\% \rightarrow 1.48\% (-23\%), \quad |\mathbf{q}| : 1.35\% \rightarrow 1.06\% (-21\%).$$

With the Helmholtz split in place, moving from dual-layer to single-layer increases the best-approximation error as

$$q_x : 0.86\% \rightarrow 1.01\% (+17.4\%), \quad q_y : 1.21\% \rightarrow 1.48\% (+22.3\%), \quad |\mathbf{q}| : 0.80\% \rightarrow 1.06\% (+32.5\%).$$

Conditioning worsens much more than approximation. For q_x , the div-free block increases from 2.6×10^8 to 1.2×10^{13} , while the curl-free block increases from 6.3×10^6 to 8.0×10^{12} , and similar

increases occur for q_y . Without the Helmholtz split, moving from dual-layer to single-layer increases the best-approximation error as

$$q_x : 1.00\% \rightarrow 1.29\% (+29.0\%), \quad q_y : 1.66\% \rightarrow 1.92\% (+15.7\%), \quad |\mathbf{q}| : 1.10\% \rightarrow 1.35\% (+22.7\%).$$

The condition number increases from 2.6×10^8 to 1.7×10^{15} . The mass-flux projection errors are a few orders of magnitude larger than the pressure projection errors, although they remain practically small for general Darcian applications, as summarized in Fig. S2f and Fig. S1d. This gap is expected because \mathbf{q} is not as smooth as the pressure field. The flux depends on spatial derivatives of pressure and on the multiscale permeability, so gradients amplify high-frequency content and heterogeneous $\kappa(\mathbf{x})$ injects small-scale variation into \mathbf{q} even when p remains relatively smooth. The finite-volume reference also contains grid-level high-frequency numerical content from discrete gradients, fluxes, and truncation effects, and such components are difficult for a global neural basis space to match in general. The energy spectra make this explicit in Fig. S2g. The projected and reference spectra agree closely over the dominant low-to-intermediate wavenumbers, while the remaining difference concentrates in the high-wavenumber tail, consistent with reduced smoothness and increased sensitivity to multiscale heterogeneity and discretization-induced fine-scale numerical content.

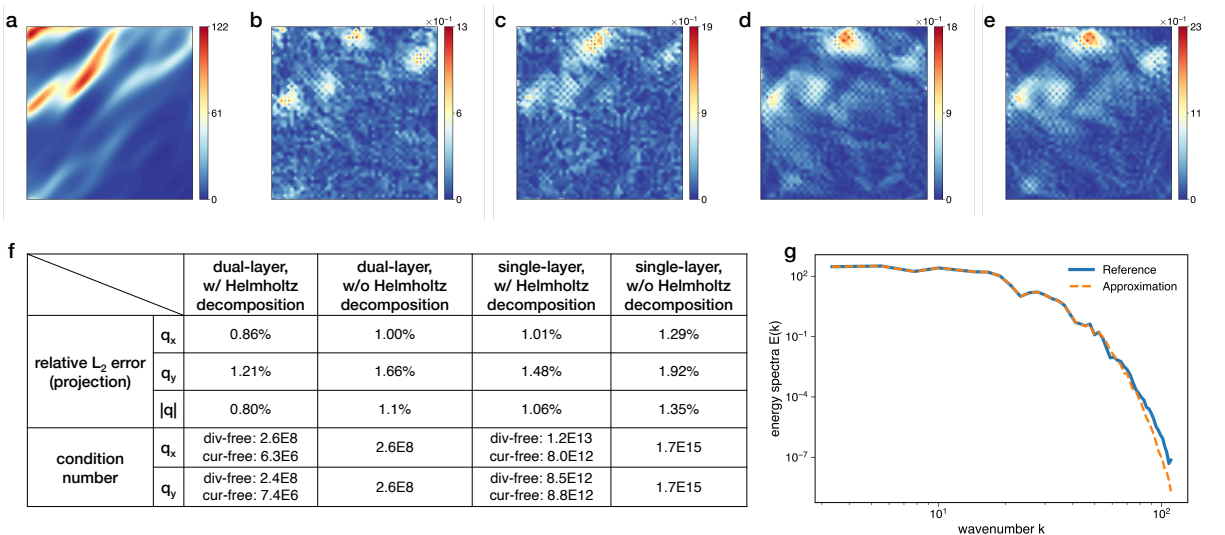


Fig. S2 | Neural basis expressivity and stability for mass-flux. **a**, FVM reference ($\text{kg m}^{-2} \text{s}^{-1}$). **b-e**, Absolute projection error using dual-layer neural vector basis w/ Helmholtz decomposition, dual-layer neural vector basis w/o Helmholtz decomposition, single-layer neural vector basis w/ Helmholtz decomposition, and single-layer neural vector basis w/o Helmholtz decomposition, respectively. **f**, Relative L_2 projection errors for q_x , q_y , and $|\mathbf{q}|$ and condition numbers of the corresponding projection systems. **g**, Energy spectra $E(k)$ of the reference and the best projected mass-flux fields. **Note:** Mass-flux is reported in $\text{kg day}^{-1} \text{m}^{-2}$.

Concentration projection: dual-layer versus single-layer basis and the effect of stabilization. Concentration projection behaves differently from pressure and mass flux. A sharp advective front limits best-approximation for smooth neural bases, while stabilization makes the target compatible with the basis and reduces projection error markedly. The FVM reference concentration, the corresponding projection errors for the dual-layer and single-layer bases, and the error-conditioning summary appear in Fig. S3a-d. Moving from the dual-layer to the single-layer basis increases the best-approximation error from 0.92% to 0.99%. Moving from the dual-layer to

the single-layer basis increases the condition number from 2.6×10^8 to 1.7×10^{15} , about 6.8 orders of magnitude, as summarized in Fig. S3d. The concentration field in a purely advective equation can develop limited regularity and sharp fronts, and the solution is naturally interpreted in a weak sense. Such interfaces are difficult for a smooth neural expansion to approximate, and direct projection of a step front produces a larger best-approximation error in Fig. S3e,g,i,k. The NBM transport discretization uses a control-volume-like form with first-order upwinding, which provides numerical stabilization by introducing a small grid-scale transition zone that mildly smears the front while preserving the propagation direction. This stabilization changes the representational target from a discontinuous step to a profile with finite transition thickness, which is compatible with neural bases. Consistent with this mechanism, projecting a slightly smeared front with a five-cell transition reduces the best-approximation error dramatically in Fig. S3f,h,j,k. The localized residual patterns in Fig. S3g–h show that the remaining discrepancy concentrates near the stabilized interface. Fig. S3k highlights an instructive interface effect. Interestingly, the sharp-front field in Fig. S3e and the slightly smeared field with a five-cell transition in Fig. S3f appear visually similar, yet their relative L_2 difference is 9.19%. The best-approximation error of projecting the discontinuous front onto the smooth neural basis is 7.73%, which is smaller than the L_2 gap between the sharp and smeared targets. Overall, Fig. S3 shows that transport benefits from stabilization, and the neural basis represents the stabilized transport solution with low error.

Helmholtz decomposition of a discrete vector field on a non-periodic box. Given a discrete vector field such as mass-flux $\mathbf{q} = (q_x, q_y)$ sampled on a regular $N_x \times N_y$ grid over a rectangular domain $\Omega = [0, L_x] \times [0, L_y]$, we compute a Helmholtz decomposition in the form

$$\mathbf{q} = \nabla\phi + \mathbf{w}, \quad \nabla \cdot \mathbf{w} = 0,$$

where $\nabla\phi$ is the curl-free component and \mathbf{w} is the divergence-free component. Because Ω has a boundary, the decomposition is not unique unless a boundary convention is specified; we adopt the standard no-penetration convention for the divergence-free part, $\mathbf{w} \cdot \mathbf{n} = 0$ on $\partial\Omega$, which implies $(\nabla\phi) \cdot \mathbf{n} = \mathbf{q} \cdot \mathbf{n}$ on $\partial\Omega$. Taking the divergence of $\mathbf{q} = \nabla\phi + \mathbf{w}$ and using $\nabla \cdot \mathbf{w} = 0$ yields a Poisson problem for the scalar potential,

$$\Delta\phi = \nabla \cdot \mathbf{q} \quad \text{in } \Omega, \quad \partial_n\phi = \mathbf{q} \cdot \mathbf{n} \quad \text{on } \partial\Omega.$$

In our experiment for investigating neural vector basis, $\nabla \cdot \mathbf{q}$ is approximated by second-order central differences in the interior and one-sided differences on the boundary. The Neumann boundary condition is enforced by eliminating ghost values in the discrete Laplacian, resulting in an equivalent right-hand-side correction on boundary-adjacent nodes. Since the pure Neumann Poisson problem determines ϕ only up to an additive constant, we fix the gauge by imposing a zero-mean condition on ϕ (equivalently, projecting the linear system onto the zero-mean subspace). The curl-free component is then reconstructed as $\mathbf{q}^{(\text{curl})} = \nabla\phi$ using the same finite-difference operators (with boundary normal derivatives consistent with $\partial_n\phi = \mathbf{u} \cdot \mathbf{n}$), and the divergence-free component is obtained by subtraction, $\mathbf{q}^{(\text{div})} = \mathbf{q} - \mathbf{q}_{\text{cf}}$. Both $\mathbf{q}^{(\text{curl})}$ and $\mathbf{q}^{(\text{div})}$ are returned on the same $N_x \times N_y$ grid as the input field, and $\mathbf{q}^{(\text{div})}$ satisfies a discrete divergence-free condition while exhibiting zero normal flux through the domain boundary by construction.

4 Geometric interpretation of dual-layer neural basis

The geometric interpretations of neural bases is briefly discussed in **Methods**. We recall the key points. With $\sigma = \tanh$, each first-layer node $\phi_j^{(1)}(\mathbf{x}) = \sigma(\mathbf{w}_j \cdot (\mathbf{x} - \mathbf{x}_c) + b_j)$ is organized around the

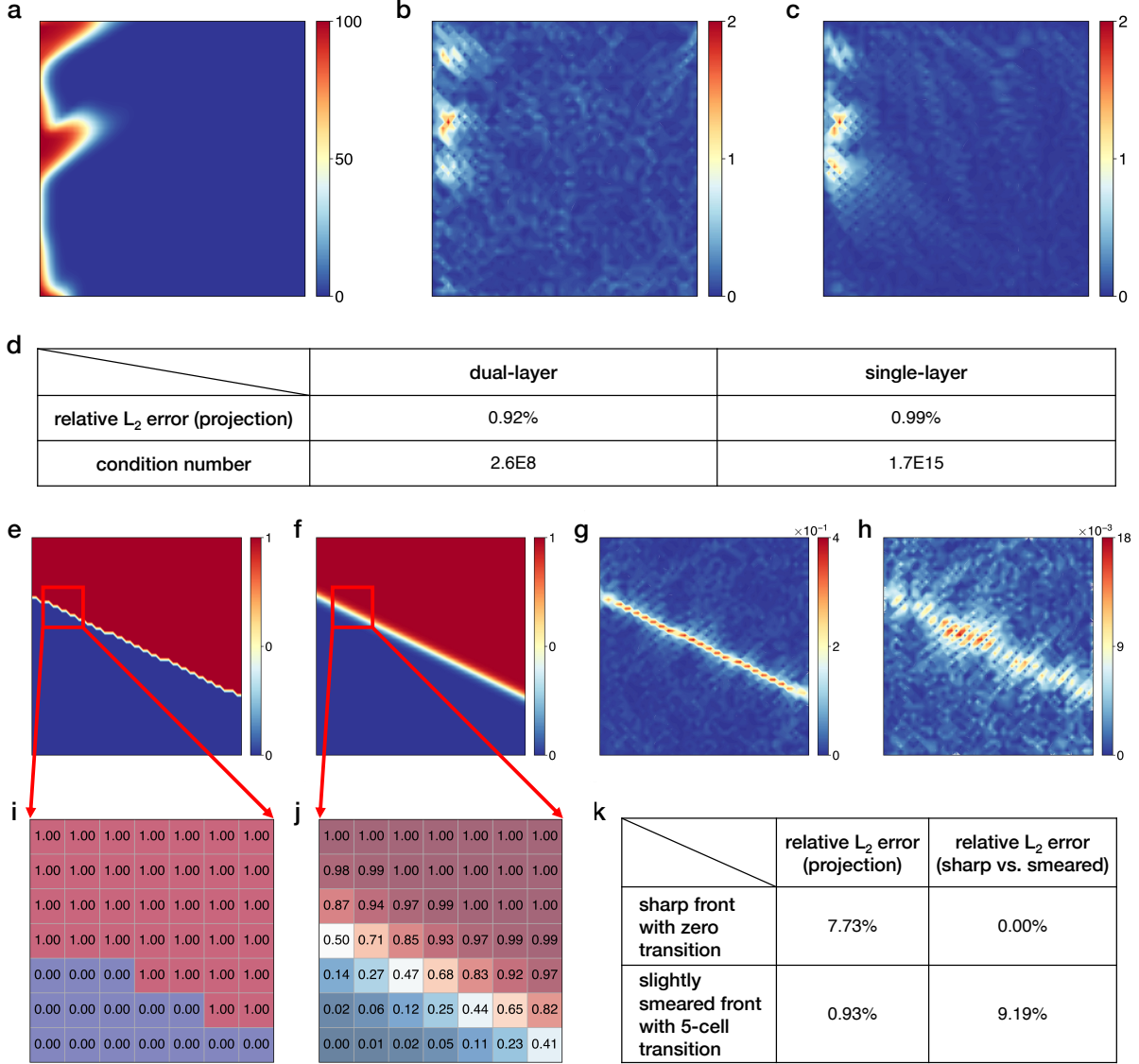


Fig. S3 | Neural-basis expressivity and stability for concentration. **a**, FVM reference. **b-c**, Absolute projection error using dual-layer and single neural scalar basis, respectively. **d**, Relative L_2 projection error and condition number of the projection system. **e**, Sharp-front field with zero transition thickness (discontinuous step). **f**, Slightly smeared front with a 5-cell transition (stabilized profile). **g-h**, Absolute projection error for sharp-front and smeared-front cases, respectively. **i-j**, Cell values near sharp-front and smeared-front, respectively. **k**, Relative L_2 projection errors for the sharp-front and smeared-front fields, and the relative L_2 difference between the two fields (sharp vs. smeared). **Note:** Concentration is reported in ppm.

characteristic hyperplane $\{\mathbf{x} : \mathbf{w}_j \cdot (\mathbf{x} - \mathbf{x}_c) + b_j = 0\}$. Here $\mathbf{x}_c \in \mathbb{R}^d$ is a fixed centering point (e.g., the domain center), $\mathbf{w}_j \in \mathbb{R}^d$ and $b_j \in \mathbb{R}$ are fixed (randomly sampled) first-layer weights and bias, and $j = 1, \dots, N_1$ indexes the N_1 first-layer nodes. A random ensemble of such hyperplanes yields a statistically uniform, hyperplane-induced soft partition of the domain: across each hyperplane the feature transitions rapidly (but smoothly). A random draw can produce near-duplicate hyperplanes, leading to highly correlated feature columns. This can make the least-squares projection matrices ill-conditioned and amplify numerical errors. To mitigate while retaining the hyperplane-induced geometry, we introduce a second fixed linear–nonlinear map and interpret it as constructing a neural

superposition of the first-layer partition. Specifically, each second-layer node $k = 1, \dots, N_2$, defines a pre-activation field

$$z_k(\mathbf{x}) = \sum_{j=1}^{N_1} W_{kj}^{(2)} \phi_j^{(1)}(\mathbf{x}) + b_k^{(2)}, \quad (\text{S2})$$

and its corresponding second-layer basis function

$$\phi_k^{(2)}(\mathbf{x}) = \sigma(z_k(\mathbf{x})). \quad (\text{S3})$$

Here $W_{kj}^{(2)}$ and $b_k^{(2)}$ are fixed (randomly sampled) second-layer weights and bias, and $\sigma(\cdot)$ acts on the scalar field $z_k(\mathbf{x})$. Equation (S2) shows that $z_k(\mathbf{x})$ is a fixed superposition of the hyperplane-induced soft partitions produced by the first layer. Because each $\phi_j^{(1)}$ contributes a localized transition across its characteristic hyperplane, the superposition z_k can be viewed as an aggregated partitioning effect formed by many hyperplane-induced transitions. We refer to this aggregated field $z_k(\mathbf{x})$ as a soft neural discretization signal: its level sets and transition regions encode a composite soft partition formed by the superimposed hyperplane responses. Applying σ in (S3) then performs a bounded nonlinear transformation of this discretization signal, which (i) preserves the geometric organization inherited from the first-layer partition, while (ii) improving conditioning by reducing collinearity. Finally, the PDE solution is represented by an output-layer linear combination of $\{\phi_k^{(2)}\}$. In our implementation, we draw each row of $\mathbf{W}^{(2)} = [W_{kj}^{(2)}] \in \mathbb{R}^{N_2 \times N_1}$ from a Gaussian distribution and sample $\mathbf{b}^{(2)} = (b_1^{(2)}, \dots, b_{N_2}^{(2)})^\top \in \mathbb{R}^{N_2}$ uniformly in a prescribed interval (e.g., $[-1.5, 1.5]$), then keep all parameters frozen. Fig. S4 provides an illustrative visualization: we plot (i) representative pre-activation fields $z_k(\mathbf{x})$ that expose the superimposed hyperplane-induced discretization, and (ii) the corresponding post-activation basis functions $\phi_k^{(2)}(\mathbf{x}) = \sigma(z_k(\mathbf{x}))$. Although the dual-layer basis is not trained, it yields substantially better-separated features and dramatically improved conditioning in the resulting projection systems compared with using $\{\phi_j^{(1)}\}$ directly, while retaining an interpretable geometric link to the first-layer hyperplane partition. In this sense, depth in the basis generator primarily serves numerical stability and geometric organization, rather than increasing expressivity through training.

To provide an illustrative visualization of the dual-layer geometric interpretation, we show (i) a representative first-layer feature $\phi_j^{(1)}(\mathbf{x})$ after activation that induces a partition of the domain via the hyperplane (Fig. S4a), and (ii) representative second-layer pre-activation fields $z_k(\mathbf{x}) = \sum_{j=1}^{N_1} W_{kj}^{(2)} \phi_j^{(1)}(\mathbf{x}) + b_k^{(2)}$, which explicitly expose the superposition of many hyperplane-induced transitions and thus form a composite “neural discretization” (Fig. S4b–c, shown for $N_1 = 10$ for clarity and for $N_1 = 200$ to illustrate a finer superposition). Fig. S4d places this view in a standard fully connected feedforward network diagram. Thick red connections highlight how first-layer hyperplane features are superposed to form z_k , and applying the activation produces the corresponding post-activation basis function $\phi_k^{(2)}(\mathbf{x}) = \sigma(z_k(\mathbf{x}))$ that enters the final expansion. This dual-layer architecture with the fixed linear–nonlinear recombination yields dramatically improved conditioning in the resulting projection systems compared with using $\{\phi_j^{(1)}\}$ directly, while retaining a clear geometric link to the first-layer hyperplane partition.

5 Effect of dual-layer neural basis in conditioning

We empirically quantify the numerical conditioning of the neural projection system as the basis size (N_b) increases, by tracking the condition number of the resulting linear system (assembled

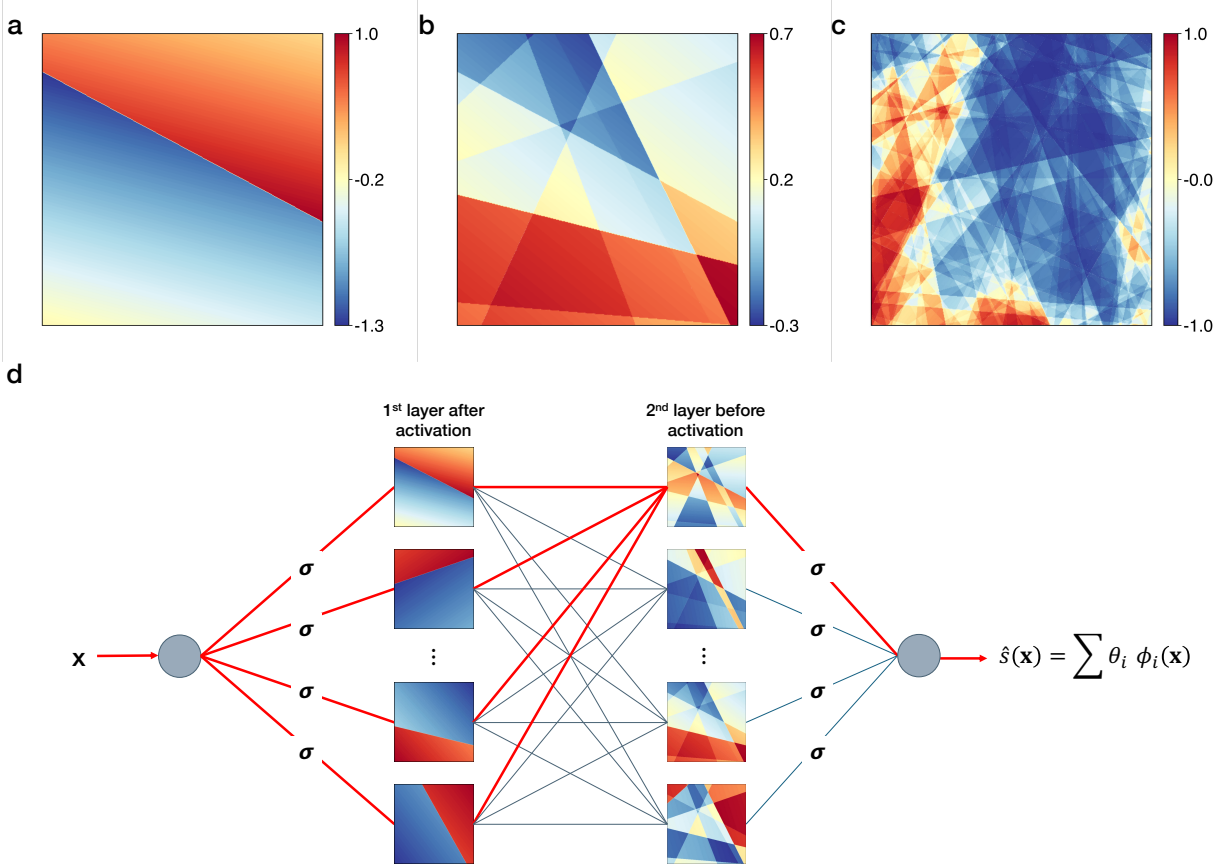


Fig. S4 | Geometric illustration of dual-layer neural basis architecture. **a**, A representative first-layer hyperplane feature after activation. **b**, A representative second-layer pre-activation field formed by superposing $N_1 = 10$ first-layer features. **c**, A representative second-layer pre-activation field formed with $N_1 = 200$ first-layer features. **d**, Schematic of the dual-layer basis generator: input produces first-layer hyperplane features, superpositions form pre-activations field, and post-activation outputs the final basis functions. Thick red connections highlight the illustrative path from first-layer features through a second-layer superposition to a single output basis function.

from the same weighted least-squares formulation) for three basis generators: a single-layer basis, a dual-layer basis, and a triple-layer basis. The underlying system is based on the model setup of Fig. 3a. Fig. S5 reports the condition number versus N_b on a semi-log scale. The single-layer basis becomes rapidly ill-conditioned as N_b grows, with the condition number increasing in the exponential-like trend (up to $N_b = 1000$) and reaching 3.34×10^{13} at $N_b = 1000$. Such a condition number is sufficiently large to severely degrade the reliability of the least-squares solution, making the fitted coefficients highly sensitive to numerical noise (e.g., finite-precision roundoff) and small perturbations in the assembled system. In contrast, introducing one additional hidden layer (dual-layer) substantially improves conditioning across the entire tested range of N_b , yielding 5.76×10^8 at $N_b = 1000$ (a ~ 6 -order reduction relative to the single-layer case). Adding a third layer further stabilizes the system and keeps the conditioning at 9.25×10^6 at $N_b = 2000$ (a ~ 11 -order reduction relative to the single-layer case, and ~ 3 orders relative to the dual-layer case). Overall, depth consistently mitigates the growth of condition number with N_b , enabling larger neural spaces to be used before numerical stability becomes limiting. For the dual- and triple-layer generators, we choose all hidden layers to have the same width. This design choice is not required in principle, but it provides a controlled and fair comparison across depths: it removes confounding effects from asymmetric bottlenecks or width imbalance, keeps the architecture isotropic as N_b scales, and

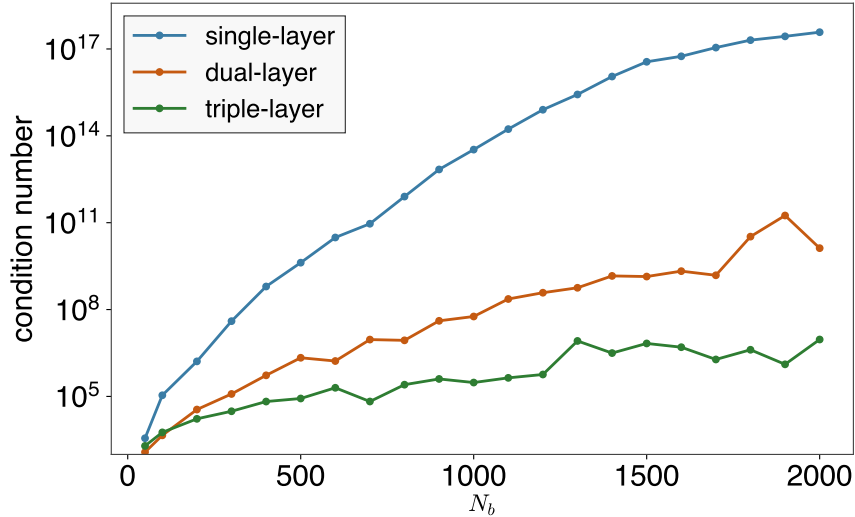


Fig. S5 | Effect of depth in neural basis generation on numerical conditioning. Condition number of the assembled neural projection system versus neural basis size N_b for single-layer, dual-layer, and triple-layer basis generators (logarithmic y -axis). For dual- and triple-layer generators, all hidden layers are chosen to have identical width to avoid width-asymmetry/bottleneck effects and to isolate the contribution of depth to conditioning.

makes the parameter growth with respect to N_b consistent across the dual- and triple-layer families. Under this controlled setting, the conditioning trends can be attributed primarily to the effect of depth on the induced basis correlations, rather than to an incidental choice of layer-wise widths.

A complementary geometric interpretation helps contextualize why basis counts in the range $N_b \sim 10^3$ already provide enormous spatial partitioning in the physical dimensions most relevant to engineering system PDEs in a spatial domain of \mathbb{R}^d ($d = 1-3$). For a single hidden layer, each neuron introduces a hyperplane partition in the input space. If N_1 hyperplanes are in general position (which occurs with probability one under continuous random sampling), then the maximum number of partitions (P_d) into which \mathbb{R}^d (and likewise any bounded convex subdomain such as a line segment, disk, or ball) is partitioned is

$$P_d(N_1) = \sum_{k=0}^d \binom{N_1}{k}.$$

Hence, in $d = 1$, $R_1(N_1) = N_1 + 1$; in $d = 2$, $R_2(N_1) = 1 + N_1 + \binom{N_1}{2}$; and in $d = 3$, $R_3(N_1) = 1 + N_1 + \binom{N_1}{2} + \binom{N_1}{3}$. For example, $N_1 = 1000$ yields $R_1 = 1001$, $R_2 = 500,501$, and $R_3 = 166,667,501$ partitions; while $N_1 = 2000$ yields $R_1 = 2001$, $R_2 = 2,001,001$, and $R_3 = 1,333,335,001$ partitions. These numbers indicate that in low-dimensional physical spaces (spatially $d = 1-3$), a thousand first-layer hyperplanes already can induce sufficiently fine domain partitioning, suggesting that representational power from “raw partition count” is unlikely to be the bottleneck beyond $N_b = O(10^3)$. Instead, the practical limitation is the numerical conditioning of the projection system, which motivates deeper generators that produce a better-conditioned neural basis while maintaining expressive capacity.

6 Effect of physics-conforming neural vector bases

We assess the effect of the proposed physics-conforming neural vector basis (constructed via a Helmholtz-type decomposition) by comparing NBM runs with and without this structure for both

the homogeneous and heterogeneous CO₂ storage settings (Fig. 2a and Fig. 3a), where system is compressible. As summarized in Fig. S6, we report (i) the conservative residuals measured from the least-squares solve, and (ii) relative L_2 errors/differences for pressure (q), velocity (u_x and u_y), and concentration (c). The conservation residual is computed from the fitted least-squares residual vector after solving the neural-discretized system. Let $\mathcal{E} = \mathbf{A}\boldsymbol{\theta}^* - \mathbf{b}$, where $\boldsymbol{\theta}^*$ is the least-squares solution. We extract the entries of \mathcal{E} associated with the conservation (mass-balance) equations and compute their squared L_2 norm; the reported value in Fig. S6 is the normalized quantity $\mathcal{E}_{\text{rel}}^{\text{cons}} = \|\mathcal{E}_{\text{cons}}\|_2^2 / \|\mathbf{b}\|_2^2$. This normalization makes comparable across configurations. For the heterogeneous case, we intentionally denote the comparison as relative L_2 differences (rather than errors) because a mesh-converged ground truth is not available for heterogeneous fields based on discrete-valued realizations. We therefore use an FVM solution on the same spatial resolution as the NBM discretization as the reference baseline. Overall, Fig. S6 shows that enforcing the physics-conforming vector structure substantially reduces conservative residuals and improves downstream transport solution quality, with strong gains observed in the heterogeneous setting. It should be noted that, in incompressible situations, the benefit of a physics-conforming vector basis is immediate: the divergence-free physics is represented exactly by this construction, which can eliminate the need to include a separate conservation equation in the least-squares system (assuming any source/sink terms are imposed as internal boundary conditions).

		conservative residual	p (%)	u_x (%)	u_y (%)	c (%)	spectral (%)	K-S distance
Homogeneous (Fig. 2a)	w/ physics-conforming	9.92E-12	0.001	0.16	0.30	5.17	0.02	2.45E-5
	w/o physics-conforming	1.34E-9	0.0016	0.12	0.35	5.30	0.03	2.48E-5
Heterogeneous (Fig. 3a)	w/ physics-conforming	6.17E-11	0.045	1.96	3.03	4.09	0.91	0.002
	w/o physics-conforming	7.93E-8	0.11	3.89	5.18	8.70	4.69	0.003

Fig. S6 | Effect of physics-conforming neural vector bases.

7 Construction of physics-conforming neural vector bases for 3D

Given scalar neural basis functions $\{\phi_i(\mathbf{x})\}$ in $\Omega \subset \mathbb{R}^3$, we define the 3D curl-free neural vector basis by

$$\phi_i^{(\text{curl})}(\mathbf{x}) = \nabla \phi_i(\mathbf{x}) = \begin{bmatrix} \partial_x \phi_i(\mathbf{x}) \\ \partial_y \phi_i(\mathbf{x}) \\ \partial_z \phi_i(\mathbf{x}) \end{bmatrix}.$$

To construct a divergence-free basis from the same scalar features, we use a vector-potential representation. For each scalar feature ϕ_i , we introduce three fixed embeddings into a vector potential,

$$\mathbf{F}_i^{(x)}(\mathbf{x}) = \mathbf{e}_x \phi_i(\mathbf{x}), \quad \mathbf{F}_i^{(y)}(\mathbf{x}) = \mathbf{e}_y \phi_i(\mathbf{x}), \quad \mathbf{F}_i^{(z)}(\mathbf{x}) = \mathbf{e}_z \phi_i(\mathbf{x}),$$

with $\mathbf{e}_x = (1, 0, 0)^\top$, $\mathbf{e}_y = (0, 1, 0)^\top$, and $\mathbf{e}_z = (0, 0, 1)^\top$. We then define three solenoidal basis families by taking curls,

$$\phi_i^{(\text{div},x)}(\mathbf{x}) = \nabla \times \mathbf{F}_i^{(x)}(\mathbf{x}), \quad \phi_i^{(\text{div},y)}(\mathbf{x}) = \nabla \times \mathbf{F}_i^{(y)}(\mathbf{x}), \quad \phi_i^{(\text{div},z)}(\mathbf{x}) = \nabla \times \mathbf{F}_i^{(z)}(\mathbf{x}),$$

which yield the explicit forms

$$\phi_i^{(\text{div},x)}(\mathbf{x}) = \begin{bmatrix} 0 \\ \partial_z \phi_i(\mathbf{x}) \\ -\partial_y \phi_i(\mathbf{x}) \end{bmatrix}, \quad \phi_i^{(\text{div},y)}(\mathbf{x}) = \begin{bmatrix} -\partial_z \phi_i(\mathbf{x}) \\ 0 \\ \partial_x \phi_i(\mathbf{x}) \end{bmatrix}, \quad \phi_i^{(\text{div},z)}(\mathbf{x}) = \begin{bmatrix} \partial_y \phi_i(\mathbf{x}) \\ -\partial_x \phi_i(\mathbf{x}) \\ 0 \end{bmatrix}.$$

By construction, $\nabla \cdot \phi_i^{(\text{div},x)} \equiv \nabla \cdot \phi_i^{(\text{div},y)} \equiv \nabla \cdot \phi_i^{(\text{div},z)} \equiv 0$. In implementation, the 3D divergence-free coefficients are stored as three blocks $\theta^{(\text{div},x)}, \theta^{(\text{div},y)}, \theta^{(\text{div},z)} \in \mathbb{R}^{N_b}$. The divergence-free flux is reconstructed by

$$\mathbf{q}_{NN}^{(\text{div})}(\mathbf{x}) = \sum \left(\theta_i^{(\text{div},x)} \phi_i^{(\text{div},x)}(\mathbf{x}) + \theta_i^{(\text{div},y)} \phi_i^{(\text{div},y)}(\mathbf{x}) + \theta_i^{(\text{div},z)} \phi_i^{(\text{div},z)}(\mathbf{x}) \right),$$

which yields the componentwise expressions

$$\begin{aligned} q_{x,NN}^{(\text{div})}(\mathbf{x}) &= \sum \left(-\theta_i^{(\text{div},y)} \partial_z \phi_i(\mathbf{x}) + \theta_i^{(\text{div},z)} \partial_y \phi_i(\mathbf{x}) \right), \\ q_{y,NN}^{(\text{div})}(\mathbf{x}) &= \sum \left(\theta_i^{(\text{div},x)} \partial_z \phi_i(\mathbf{x}) - \theta_i^{(\text{div},z)} \partial_x \phi_i(\mathbf{x}) \right), \\ q_{z,NN}^{(\text{div})}(\mathbf{x}) &= \sum \left(-\theta_i^{(\text{div},x)} \partial_y \phi_i(\mathbf{x}) + \theta_i^{(\text{div},y)} \partial_x \phi_i(\mathbf{x}) \right). \end{aligned}$$

The curl-free flux is reconstructed as

$$\mathbf{q}_{NN}^{(\text{curl})}(\mathbf{x}) = \sum \theta_i^{(\text{curl})} \phi_i^{(\text{curl})}(\mathbf{x}) = \sum \theta_i^{(\text{curl})} \begin{bmatrix} \partial_x \phi_i(\mathbf{x}) \\ \partial_y \phi_i(\mathbf{x}) \\ \partial_z \phi_i(\mathbf{x}) \end{bmatrix},$$

i.e.,

$$q_{x,NN}^{(\text{curl})}(\mathbf{x}) = \sum \theta_i^{(\text{curl})} \partial_x \phi_i(\mathbf{x}), \quad q_{y,NN}^{(\text{curl})}(\mathbf{x}) = \sum \theta_i^{(\text{curl})} \partial_y \phi_i(\mathbf{x}), \quad q_{z,NN}^{(\text{curl})}(\mathbf{x}) = \sum \theta_i^{(\text{curl})} \partial_z \phi_i(\mathbf{x}).$$

Finally, the total flux is given by

$$\mathbf{q}_{NN}(\mathbf{x}) = \mathbf{q}_{NN}^{(\text{div})}(\mathbf{x}) + \mathbf{q}_{NN}^{(\text{curl})}(\mathbf{x}).$$

All spatial derivatives of ϕ_i are evaluated by automatic differentiation of the neural basis generator.

8 Physics-informed neural network (PINN) baseline

We use a two-network, two-stage vanilla PINN baseline for the coupled Darcy–transport problem. In Stage A, pressure is approximated by a neural network $p(\cdot; \omega_p)$, where ω_p denotes the trainable network parameters. We train ω_p by minimizing a weighted sum of mean-squared residuals at collocation points: an interior term enforcing the slightly-compressible Darcy equation in strong form, plus boundary penalty terms enforcing a left Dirichlet pressure constraint and mass-flux constraints on the remaining boundaries, where the normal mass flux is obtained from ∇p via automatic differentiation. Stage A optimization uses Adam with mini-batched collocation points followed by full-batch L-BFGS refinement.

In Stage B, concentration is approximated by a second network $c(\cdot; \omega_c)$, where ω_c denotes its trainable parameters. We freeze ω_p and train ω_c using a conservative mass-flux transport residual evaluated at space–time collocation points, together with penalties for the initial condition $c(\cdot, 0) =$

0 and a time-dependent inlet Dirichlet condition on the left boundary. To reduce cost while retaining coupling at the PDE level, after Stage A converges we precompute the mass-flux components and their divergence induced by $p(\cdot; \omega_p)$ on the full space–time collocation set once; Stage B then reuses these cached fields so that each transport iteration differentiates only $c(\cdot; \omega_c)$.

Both $p(\cdot; \omega_p)$ and $c(\cdot; \omega_c)$ are fully-connected MLPs with tanh activations, taking (x, y, t) as input and outputting a scalar; each uses width 64 and depth 4. We collocate on a fixed 50×50 spatial grid of cell centers and $N_t = 10$ time levels, giving $N_{\text{all}} = 50 \times 50 \times 10$ interior space–time points; boundary collocation points are the boundary cell centers replicated across the same N_t time levels.

For Stage A, we use Adam (learning rate 10^{-3}) for 20,000 iterations with mini-batches of size 4096 (interior) and 1024 for each boundary set, followed by full-batch L-BFGS for 2,000 iterations (strong Wolfe line search; history size 30; tolerance_grad 10^{-10} ; tolerance_change 10^{-12}), where the Stage-A loss weights are $(w_{\text{pde}}, w_L, w_R, w_B, w_T) = (1, 1, 1, 1, 10)$ with w_{pde} weighting the Darcy PDE residual, and w_L, w_R, w_B, w_T weighting the left Dirichlet and right/bottom/top mass-flux boundary penalties, respectively. For Stage B (transport), we use Adam (learning rate 10^{-3}) for 10,000 iterations with mini-batches of size 4096 (interior), 1024 (initial condition), and 1024 (inlet), followed by full-batch L-BFGS for 2,000 iterations with the same settings, where the Stage-B loss weights are $(w_{\text{pde}}^{(c)}, w_{\text{ic}}, w_{\text{in}}) = (1, 0.01, 10)$ with $w_{\text{pde}}^{(c)}$ weighting the transport PDE residual, and $w_{\text{ic}}, w_{\text{in}}$ weighting the initial-condition and inlet-condition penalties. For the multiscale cases, we use 50,000 Adam iterations followed by 20,000 L-BFGS iterations for both Stage A and B training. Fig. S7 provides the respective training histories.

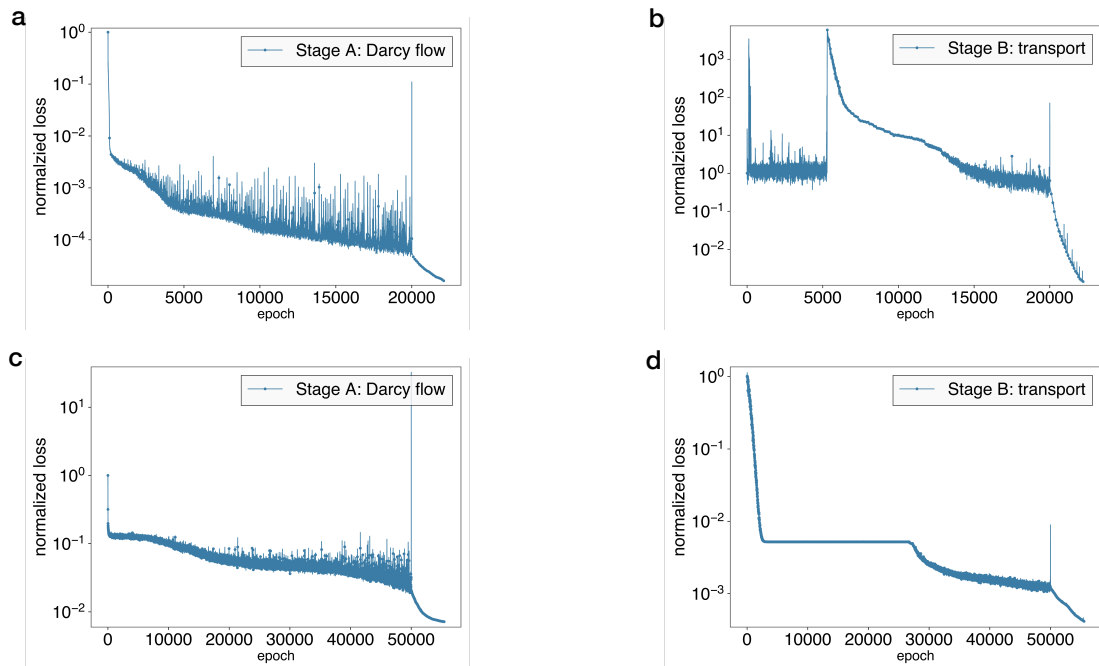


Fig. S7 | PINN training history for coupled Darcy flow and transport. **a**, Normalized training loss for Stage A (homogeneous). **b**, Normalized training loss for Stage B (homogeneous). **c**, Normalized training loss for Stage A (multiscale). **d**, Normalized training loss for Stage B (multiscale).

9 NBM-OL implementation details and experiment configurations

9.1 Common implementation details

Unless otherwise stated, all three NBM-OL experiments share the following numerical and training settings.

Domain and reporting units. All experiments use the square domain $\Omega = [0, 762] \text{ m} \times [0, 762] \text{ m}$. Pressure is reported in bar. Flux quantities are reported in the units used by the corresponding governing equation (see each experiment below).

Collocation and residual evaluation. We evaluate interior residuals on a structured 100×100 collocation set (10,000 points). Boundary residuals are evaluated on uniformly spaced points on each edge with corners excluded (total 400 boundary points). Pressure, mass-flux (or velocity for the incompressible case), and concentration are represented using separate neural bases. All the neural bases are of size $N_b = 800$.

POD compression. When POD is used, we apply it to the assembled coefficient snapshots in each coefficient block separately (e.g., div/pressure, div/curl/pressure, or concentration). We retain a fixed number of modes per block as specified for each experiment. Operator learning is performed in the corresponding reduced coordinate system.

Residual-based self-supervised training. All NBM-OL models are trained by minimizing the residual metric \mathcal{E}_{rel} evaluated in the reduced coordinate system.

OOD evaluation protocol. OOD tests are constructed by extending one or more axes of the parameter space and/or the time horizon beyond the training ranges.

9.2 Case-I: permeability-varying steady Darcy flow operator

Boundary conditions. We impose mixed pressure/flux boundary conditions (Fig. 5a): $p = 69 \text{ bar}$ on $x = 0$, $u_x = 0.3 \text{ m day}^{-1}$ on $x = 762 \text{ m}$, and $u_y = 1.5 \text{ m day}^{-1}$ on $y = 0$ and $y = 762 \text{ m}$ (outward-normal sign convention).

Permeability parameterization. The base permeability template $\kappa_{\text{ref}}(\mathbf{x})$ (units: Darcy) is defined on a 100×100 grid (Fig. 5a). Heterogeneity parameterization is introduced by a piecewise-constant 5×5 blockwise field (block25) generated from a Gaussian random field (GRF) model. A block25 realization is upsampled by block repetition to the 100×100 grid and applied multiplicatively to $\kappa_{\text{ref}}(\mathbf{x})$ to form $\kappa(\mathbf{x})$.

Dataset. We generate $N_s = 1000$ block25 realizations and compute steady NBM coefficient snapshots $(\boldsymbol{\theta}_{\text{div}}, \boldsymbol{\theta}_p)$. Here we denote velocity coefficient as $(\boldsymbol{\theta}_{\text{div}}$ because for this incompressible setup, we only need to keep the divergence-free part of the neural vector basis.

POD latent dimension. We retain $r_p = 16$ and $r_q = 16$ modes, yielding $\mathbf{z} = [\mathbf{z}_p; \mathbf{z}_q] \in \mathbb{R}^{32}$.

MLP hyperparameters. We use a two-branch MLP (pressure/velocity branches), each with two hidden layers (width 64, tanh). Training uses Adam (10^{-3}), batch size 16, for 500 epochs.

OOD tests. OOD block25 realizations are generated by perturbing the GRF controls (variance/contrast scaling, correlation length changes, and rotation-angle shifts).

9.3 Case-II: boundary-flux-varying Darcy flow operator

Parameter and boundary conditions. The operator family is parametrized by a scalar top-boundary mass-flux control g_{top} (constant along $y = 762$ m), while all other boundary values are fixed. We prescribe $p = 103$ bar on $x = 0$ and impose no-flux on the right and bottom boundaries. We sample

$$g_{\text{top}} \sim \mathcal{U}(488, 976) \text{ kg day}^{-1} \text{ m}^{-2}.$$

Permeability. We use a fixed multiscale permeability field $\kappa(\mathbf{x})$ (units: Darcy) on a 100×100 grid.

Dataset and time stepping. We generate $N_s = 200$ scenarios, each simulated for $N_{\text{Darcy}} = 20$ Darcy time steps with $\Delta T = 10.0$ days. This yields $N_{\text{snap}} = N_s N_{\text{Darcy}} = 4000$ coefficient snapshots per coefficient block $(\boldsymbol{\theta}_{\text{div}}, \boldsymbol{\theta}_{\text{curl}}, \boldsymbol{\theta}_p)$.

POD latent dimension. We apply POD to the structured coefficient blocks and retain $r_{\text{div}} = 8$, $r_{\text{curl}} = 8$, and $r_p = 8$ modes, yielding $\mathbf{z} = [\mathbf{z}_{\text{div}}; \mathbf{z}_{\text{curl}}; \mathbf{z}_p] \in \mathbb{R}^{24}$.

MLP hyperparameters. We use three MLP branches mapping (g_{top}, t) to the corresponding latent blocks, each with two hidden layers (width 32, tanh). Training uses Adam (10^{-3}), batch size 16, for 500 epochs.

OOD tests. We evaluate OOD generalization by (i) extending g_{top} by a 50% range beyond the training interval, and (ii) extending the prediction horizon by 100% beyond the training time window.

9.4 Case-III: boundary-flux/concentration-varying Darcy–transport operator

Parameters. The coupled operator family is parametrized by $(g_{\text{top}}, c_{\text{left}})$, where g_{top} is the top-boundary outward mass-flux control for Darcy flow and c_{left} is the left-boundary injected tracer concentration for transport. We sample $c_{\text{left}} \sim \mathcal{U}(50.0, 100.0)$ ppm. (The Darcy boundary setup and fixed permeability field are the same as Case-II unless stated otherwise.)

Dataset. We generate $N_s = 80$ independent scenarios. For each g_{top} , we query the pretrained Case-II model to obtain the Darcy time step velocity sequence. Each Darcy time step is split into $N_{\text{tr}} = 8$ transport substeps.

Time stepping. We use $N_{\text{darcy}} = 10$ Darcy coarse steps. With $N_{\text{tr}} = 8$ transport substeps per coarse step, the total number of transport substeps is $N_{\text{sub}} = N_{\text{Darcy}} N_{\text{tr}}$.

POD latent dimension. We apply POD to transport coefficient snapshots $\{\boldsymbol{\theta}_c\}$ and retain $r_c = 20$ modes, yielding $\mathbf{z}_c \in \mathbb{R}^{20}$.

MLP hyperparameters. We use a single MLP mapping $(g_{\text{top}}, c_{\text{left}}, t_{\text{norm}})$ to the standardized latent coordinate. The network uses two hidden layers (width 64, tanh) with weight normalization. Training uses Adam (5×10^{-3}), batch size 32, for 1000 epochs.

OOD tests. OOD evaluation extends (i) $(g_{\text{top}}, c_{\text{left}})$ beyond training ranges by 50%, and (ii) the prediction horizon by 100%.

10 Geostatistical permeability field generation

Permeability fields are generated using a geostatistical model commonly adopted in subsurface engineering to represent realistic geological heterogeneity. The permeability is assumed to follow a lognormal distribution, consistent with field observations, and is constructed from an underlying spatially correlated Gaussian random field.

Specifically, a zero-mean Gaussian random field $f(x, y)$ with prescribed spatial correlation is generated by filtering spatial white noise using an FFT-based spectral convolution method. An anisotropic Gaussian kernel is employed, characterized by correlation lengths ℓ_x and ℓ_y along the principal directions and a rotation angle θ , allowing control over both the scale and orientation of heterogeneity. The permeability field is then defined as $k(x, y) = \exp(\mu + f(x, y))$, which yields a strictly positive, lognormally distributed permeability. The overall level of heterogeneity is controlled by the Dykstra–Parsons heterogeneity coefficient $v \in (0, 1)$, a classical measure widely used in subsurface engineering. It is defined as $v = 1 - \frac{k_{50}}{k_{84.1}}$, where k_{50} and $k_{84.1}$ denote the median and the 84.1% percentile of the permeability distribution, respectively. For a lognormal permeability field, this definition leads to the explicit relation $\sigma = -\ln(1 - v)$, where σ^2 is the variance of the underlying Gaussian field $f(x, y)$. The mean parameter μ is chosen to match a prescribed mean permeability k_{avg} via $\mu = \ln(k_{\text{avg}}) - \frac{1}{2}\sigma^2$. This procedure produces high-resolution permeability realizations that simultaneously satisfy a prescribed mean permeability, a controlled level of heterogeneity quantified by the Dykstra–Parsons coefficient, and physically meaningful spatial correlation structures.